nature communications

Article

https://doi.org/10.1038/s41467-025-58407-z

Lactobacillus acidophilus potentiates oncolytic virotherapy through modulating gut microbiota homeostasis in hepatocellular carcinoma

Received: 16 October 2024

Accepted: 20 March 2025

Published online: 07 April 2025

Check for updates

Jiayu Zhang[1,2,3,4,10], Jinneng Yang[1,2,3,4,10], Jinyan Luo[5], Weili Wu[1,2,6], Haidan Luo[1,2,3,4], Wenxia Wei[1,2,3,4], Haimei Lyu[1,2,3,4], Yuzhi Wang[1,2,3,4], Hairong Yi[1,2,3,4], Yijing Zhang[1,2,3,4], Zongmin Fan[1,2,3,4], Haiwen Lyu[1,2,3,4], Vishnu Priya Kanakaveti[7], Baifu Qin[1,2,3,4], Ping Yuan[1,2,3,4], Runxiang Yang[8], Haipeng Zhang[9], Tao Zuo[1,2,3,4], Dean W. Felsher[7], Mong-Hong Lee[1,2,3,4] ✉ & Kai Li[1,2,3,4] ✉

Oncolytic viruses (OVs) hold promise for cancer treatment. However, the antitumor efficacy is limited. Microbiota plays a pivotal role in cancer treatment and its impact on oncolytic virotherapy is unknown. Here, we show that VSVΔ51 has higher antitumor efficacy for hepatocellular carcinoma in the absence of microbiota in female mouse models. VSVΔ51 infection causes microbiota dysbiosis, increasing most of the gut bacteria abundance, while decreasing the commensal *Lactobacillus*. VSVΔ51 reduced intestinal expression of SLC20A1 that binds to *Lactobacillus acidophilus* (*L. acidophilus*) CdpA cell wall protein through IL6-JAK-STAT3 signaling, thereby attenuating attachment and colonization of *L. acidophilus*. *L. acidophilus* supplementation confers sensitivity to VSVΔ51 through restoring gut barrier integrity and microbiota homeostasis destroyed by VSVΔ51. In this work, we show that targeting microbiota homostasis holds substantial potential in improving therapeutic outcomes of oncolytic virotherapy.

Hepatocellular carcinoma (HCC), accounting for ~75% of all liver cancers[1], is the third leading cause of cancer related deaths worldwide[2]. The development of systemic therapy for HCC has achieved great progress during the last decades, including multi-targeted tyrosine kinase inhibitors (TKIs) and immune checkpoint inhibitors (ICIs)[3]. Despite these unprecedented and encouraging results, only 20–30% of patients respond to treatment[3]. Thus, there is an urgent need to identify new therapeutics that inhibit tumorigenesis and enhances the responses in HCC.

Oncolytic virus (OVs) are viruses that preferentially replicate in and kill tumor cells while leaving non-neoplastic cells intact[4]. Oncolytic virotherapy is a potentially attractive strategy for the treatment of

[1]Guangdong Provincial Key Laboratory of Colorectal and Pelvic Floor Disease, The Sixth Affiliated Hospital, Sun Yat-sen University, Guangzhou 510655, China. [2]Guangdong Research Institute of Gastroenterology, The Sixth Affiliated Hospital, Sun Yat-sen University, Guangzhou 510655, China. [3]Key Laboratory of Human Microbiome and Chronic Diseases (Sun Yat-sen University), Ministry of Education, Guangzhou, China. [4]Biomedical Innovation Center, The Sixth Affiliated Hospital, Sun Yat-sen University, Guangzhou, China. [5]The First Affiliated Hospital of Nanjing Medical University, 300 Guangzhou Road, Nanjing 210029, China. [6]Department of Clinical Laboratory, The Sixth Affiliated Hospital, Sun Yat-sen University, Guangzhou, China. [7]Division of Oncology, Department of Medicine, Stanford University, Stanford, CA 94305, USA. [8]Department of the Second Medical Oncology, The Third Affiliated Hospital of Kunming Medical University, 519, Kunzhou Road, Kunming 650118, China. [9]Department of Pharmacology, School of Medicine, Jinan University, Guangzhou, Guangdong 510632, China. [10]These authors contributed equally: Jiayu Zhang, Jinneng Yang. ✉e-mail: limh33@mail.sysu.edu.cn; likai39@mail.sysu.edu.cn

HCC[5,6]. Many OVs are used for clinical trials in liver cancer patients[7,8]. For example, a phase II trial showed that JX-594 high-dose group increased patients' median total survival time by 7.4 months compared with the low-dose group, suggesting that JX-594 showed potential antitumor effect and good tolerance in HCC patients[9]. Vesicular stomatitis virus (VSV), a negative-strand RNA virus, also shows prominent antitumor efficacy in hepatocellular carcinoma[10–13]. However, clinical trials have shown that only a subset of patients respond well to OVs[9]. Thus, enhancing oncolytic efficacy is urgently needed. Most of the studies have mainly focused on the mechanism of OVs in the tumor microenvironment (TME)[14–18] but the interaction between OVs treatment and other organs or tissues is rarely explored.

Much evidence indicates that deregulated microbiota plays a critical role in affecting cancer progression and immunotherapy[19–25]. For example, a recent report shows that microbial metabolite enhances immune checkpoint inhibitor efficacy by modulating T cell stemness in pan-cancer[26]. Another report suggested that oral reovirus reshapes the gut microbiome and enhances antitumor immunity in colon cancer[27]. Oncolytic immunotherapy regarding microbiota deregulation and its impact on tumor microenvironment in HCC has not been reported.

Here, we show that the efficacy of oncolytic virotherapy is attenuated by the presence of microbiota and subsequent compromised antitumor immune response. Indeed, oncolytic virus VSVΔ51 treatment leads to altered gut microbiome homeostasis, reflecting that microbiota is involved in regulating the efficacy of oncolytic virotherapy. Microbiota profiling shows that specific bacteria strains changes during VSVΔ51 treatment. Especially, VSVΔ51 affect *L. acidophilus* attachment and colonization by downregulating the expression of SLC20A1, the receptor from the intestinal epithelium for *L. acidophilus*. VSVΔ51-mediated decrease of *L. acidophilus* attachment leads to the augmentation of other commensal bacteria. Supplementation of *L. acidophilus* reprogrammed microbiome homeostasis, thereby enhancing multiple OVs' antitumor effect, including VSVΔ51, HSV-1 armed with PD-1 antibody and Vaccina virus. In this work, we reveal a previously uncharacterized role of microbiota in oncolytic virotherapy, which provides a possible mechanistic basis for future strategies to improve the efficacy of oncolytic virotherapy.

Results

Gut microbiota affect the efficacy of VSVΔ51-mediated oncolytic virotherapy in HCC

To explore the role of microbiota in oncolytic virotherapy, we established subcutaneous and orthotopic liver cancer mice models (4 groups in H22, Hepa1-6) using an antibiotic cocktail (ABX) of vancomycin, cilastatin, neomycin and amphotericin to abolish the microbiota composition: (i) PBS, (ii) ABX, (iii) VSVΔ51 (OVs), (iv) VSVΔ51 plus ABX (Fig. 1a). The data shows that VSVΔ51 plus ABX group had better antitumor efficacy than VSVΔ51 in terms of decreased tumor burden and proliferation, smaller tumor area and better survival (Fig. 1b–d and Supplementary Fig. 1a). Tumors from VSVΔ51 plus ABX group had reduced Ki-67 and elevated cleaved-Caspase-3 staining (Supplementary Fig. 1b, c). H22 tumor oncolytic virotherapy experiments were performed in germ-free (GF) mice and conventional specific pathogen-free (SPF) mice. Like oral antibiotics treated mice (to abolish microbiota), oncolytic virotherapy is much more efficient in GF mice than SPF mice (Fig. 1e) in terms of relative tumor proliferation rate (T/C%) and tumor mass measurement (Fig. 1f and Supplementary Fig. 1d). Tumors from GF mice had significant reduced Ki-67 and elevated cleaved-Caspase-3 staining (Supplementary Fig. 1e). Furthermore, Fecal Microbiota Transplantation (FMT) of VSVΔ51 treated tumor-bearing mice feces ($FMT_{VSV\Delta51}$) to ABX-treated mice for oncolytic virotherapy experiments (Fig. 1g) results in compromised antitumor effect of OVs, suggesting that feces from VSVΔ51 treated tumor-bearing mice contained microbiome that reduced efficacy of oncolytic virotherapy (Fig. 1h and Supplementary Fig. 1g).

We found that VSVΔ51 replication was more efficient in tumor tissues of GF mice than that of SPF group based on VSV-G expression (Fig. 1i), suggesting that microbiota may have deferred impact on viral replication. Indeed, we found that OVs loading is significantly higher in various tissues from GF mice/ABX-treated mice than that of SPF/control mice (Fig. 1j). Notably, we found that the viral RNA accumulates in tumor samples than that of other tested organs or tissues by up to ~2000 times including heart, spleen, and lung, suggesting that the enhanced viral replication by absence/reduction of microbiome is selectively enriched in tumor (Fig. 1j). H&E staining shows that VSVΔ51 treatment did not induce significant pathology changes in major organs (heart, liver, spleen, lung, kidney, and brain) from both SPF/GF and control/ABX mice, suggesting the safety of the therapeutics (Supplementary Fig. 1h).

Oncolytic viruses can induce a potent systemic and potentially durable antitumor immunity[14,28]. We observed that the enhanced replication of VSVΔ51 induced by microbiome depletion stimulates stronger antitumor immunity. Dendritic cells (DCs) can process and present tumor antigens to T cells for initiating anti-tumor response; we then found that VSVΔ51 treatment led to more DCs infiltration in GF mice when compared with SPF mice (1.86 × vs 1.17 ×) (Fig. 1k). Next, while both GF and SPF mice do not increase the number of $CD8^+$ T cells, cytotoxic effector $CD8^+$ T cells (T_{eff}) are augmented, including Granzyme B^+ (GF mice 2.43 × vs SPF mice 1.84 ×), IFN-γ^+ (GF mice 1.33 × vs SPF mice 1.19 ×) and TNF-α^+ (GF mice 1.61 × vs SPF mice 1.43 ×) $CD8^+$ T cells. By contrast, exhausted $CD8^+$ T cells (T_{ex}) are further decreased, including PD-1^+ (GF mice 0.28 × vs SPF mice 0.59 ×), $TIGIT^+$ (GF mice 0.49 × vs SPF mice 0.76 ×) and TIM-3^+ (GF mice 0.24 × vs SPF mice 0.53 ×) $CD8^+$ T cells (Fig. 1k). Regulatory $CD4^+$ T cells (T_{reg}) were also decreased (GF mice 0.67 × vs SPF mice 0.71 ×) (Fig. 1l and Supplementary Fig. 1i).

Taken together, all these data suggest that the existence of microbiota can decrease VSVΔ51 replication and compromise oncolytic effect in mouse liver cancer models.

VSVΔ51 alters gut microbiome homeostasis including gut transit time, metabolome, and microbiota composition

Since microbiota altered by VSVΔ51 restricts the antitumor effect, we hypothesized that the physiological outcomes caused by VSVΔ51–altered gut microbiome may be related to this compromised antitumor effect (Fig. 2a). We observed that VSVΔ51 treatment significantly decreased fecal output and pellet water content, suggesting that constipation occurred (Fig. 2b). We confirmed that small intestine transit is decreased, while whole gut transit time is increased (Fig. 2c). Moreover, VSVΔ51 treatment dramatically changes microbial metabolites based on metabolomic analysis (Fig. 2d, e). Amino acid metabolism and vitamins metabolism pathways were top ranked (Fig. 2f). Therefore, these data led us to study the composition of bacteria regulated by VSVΔ51 systematically.

Microbiota composition was analyzed by 16S ribosomal RNA (rRNA) gene sequencing from the indicated mouse groups. Principal coordinate analysis (PCoA) showed that the microbiota composition of VSVΔ51 plus ABX group was significantly distinct from the control and VSVΔ51 groups (Fig. 2g). Bacteria richness and evenness were estimated using the Chao1 index. The data show that the alpha diversity was significantly increased in VSVΔ51 treatment group. Meanwhile, ABX treatment decreased the alpha diversity (Fig. 2h). Furthermore, the differentially distributed microbial community was characterized among the groups. When comparing the microbiota of VSVΔ51 treatment and non-treated mice via taxonomic profiling, we observed apparent changes at genus and phylum level (Fig. 2i). The richness of top ranked bacteria was shown (Fig. 2j, k). We performed linear discriminant analysis (LDA) effect size (LEfSe) and found that VSVΔ51

https://doi.org/10.1038/s41467-025-58407-z

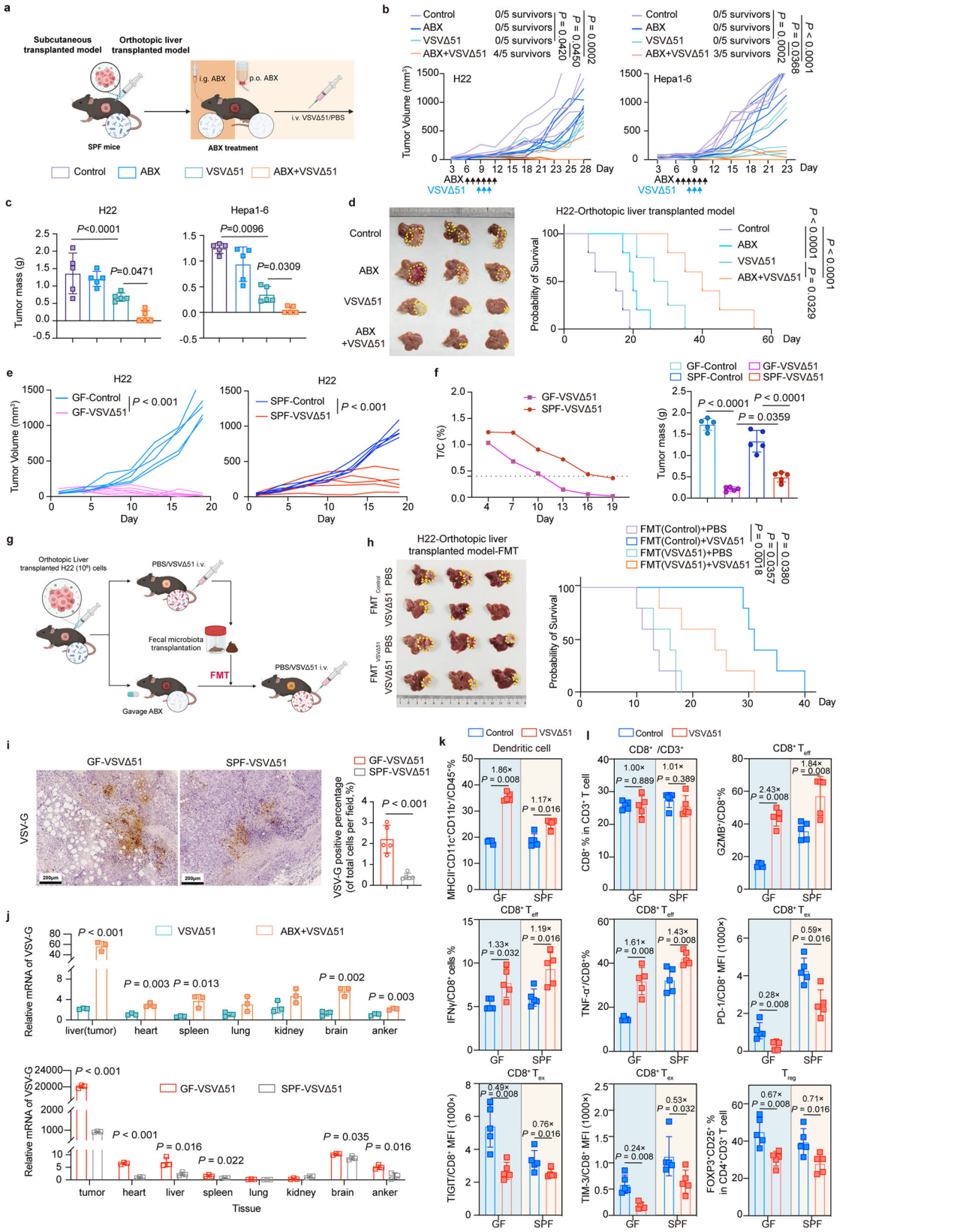

treatment increased the richness of lots of bacteria, including *Barnsiella, Clostridium_XIVa, Akkermansia, Desulfovibrio, Acetatifactor, Clostridium_IV, Alistipes* and *Rikenella*. In contrast, *Lactobacillus, Blautia* and *Klebsiella* were significantly decreased after VSVΔ51 treatment (Fig. 2l). We confirmed the observation and found that most of the bacteria could be affected by VSVΔ51 treatment in the repeated experiments, such as *Clostridium_XIVa, Acetatifactor, Clostridium_IV, Alistipes*, *Lactobacillus* and *Blautia* (Fig. 2m). Collectively, these data suggest a strong impact on the gut microbiota composition after oncolytic virotherapy.

Fig. 1 | Depletion of the microbiota enhances anti-tumor effects of VSVΔ51. **a** Schematic of the experimental design. Antibiotics (ABX) or water were intragastric (i.g.) injected 3 times and subsequently added into drinking water per os (p.o.) after tumor cells injection; VSVΔ51 were intravenously administrated (1×10^7 PFUs, i.v.) 3 times after ABX treatment. Tumor weight was calculated. Created in BioRender. Yang, X. (2025) https://BioRender.com/d33a515. **b** H22 and Hepa1-6 were subcutaneously injected into mice and tumor growth was measured ($n = 5$/group). **c** Tumor mass were shown ($n = 5$/group). **d** H22 was orthotopically injected into the liver of mice. Representative images of tumor ($n = 3$/group). Kaplan-Meier survival curves were shown ($n = 5$/group). **e** H22 tumor growth curves in GF or SPF mice ($n = 5$-6/group). **f** The relative tumor proliferation rate (T/C%) and tumor mass were shown ($n = 5$/group). **g** Schematic diagram showing administration strategies of FMT. Created in BioRender. Yang, X. (2025) https://BioRender.com/k99v786. **h** Representative images of tumor were shown. Dashed yellow lines represent tumor areas and the areas were calculated. Kaplan-Meier survival curves were shown ($n = 5$/group). **i** Immunohistochemistry analysis for the VSV-G in tumor samples (Scale bar, 200 μm). Every spot presents a mean counting number from three fields ($n = 5$/group). **j** Biodistribution of VSVΔ51 in tumor and normal tissues 3 days post infection ($n = 3$/group). **k**, **l** Comparison of dendritic cells ($F4/80^-$ $MHCII^+$ $CD11c^+$), $CD8^+$ T cells ($CD8^+$), Granzyme B^+ cells, IFN-γ+ cells and TNF-α^+ cells among $CD8^+$ T cells, mean fluorescence intensity (MFI) of PD-1^+, $TIGIT^+$ and TIM-3^+ cells among $CD8^+$ T cells and regulatory T cells ($CD25^+$ $FOXP3^+$) among $CD4^+$ T cells in the TME were presented ($n = 5$/group). **b**–**l** Unpaired, two-tailed Student's *t*-test. **c**, **f** One-way ANOVA with Tukey post-hoc test were used. **d**, **h** Kaplan-Meier survival curves, and statistical differences between curves were analyzed using the log-rank test. Results are presented as mean ± S.D. Each spot represents one subject. ns, not significant. Source data are provided in the Source Data file. See also Supplementary Fig. 1.

The presence of gut microbiome is attenuating the antitumor effect of VSVΔ51

Despite gut microbiota deregulation contributes to the tumor progression, tumor-resident microbiota is an emerging tumor component that has been documented for a variety of cancer types[29,30]. To distinguish the contribution of tumor-resident bacteria and gut microbiota in affecting the antitumor effect of VSVΔ51, we use distinct combinations of antibiotics and administration routes to selectively eliminate tumor-resident bacteria or gut microbiota according to previous report[31] (Fig. 3a). Mice with orthotopic H22 tumors were treated with (i) PBS control, (ii) intravenous ABX (i.v.), (iii) gavage ABX (i.g.), (iv) intravenous VSVΔ51, (v) a combination of intravenous VSVΔ51 plus ABX i.v., (vi) a combination of intravenous VSVΔ51 plus ABX i.g. (Supplementary Fig. 2a). We collected the feces and liver cancer tissues and performed 16S rRNA sequencing. Principal coordinate analysis (PCoA) showed that the gut microbiota composition of (ABX i.g.) co-clustered with the VSVΔ51 plus ABX i.g. samples very well but was significantly distinct from the other four groups (Supplementary Fig. 2b). However, due to the abundance of microbiome in liver is relatively low, all of the six groups from liver tumors were co-clustered (Supplementary Fig. 2b). Next, alpha diversity analysis shows that ABX (i.g.) can eliminate both gut and tumor-resident microbiota. However, ABX (i.v.) majorly eliminates tumor-resident microbiota while the gut microbiota is left intact (Fig. 3b). Bacteria composition analysis confirmed that ABX (i.g.) can eliminate both gut microbiota and tumor-resident microbiota when compared with ABX (i.v.), which only eliminate tumor-resident microbiota (Fig. 3c, d, Supplementary Fig. 2c and 2d). We next tested the localization of bacteria in the liver cancer by 16S fluorescence in situ hybridization (FISH) analysis. We observed that VSVΔ51 treatment increased the tumor-resident bacteria. Importantly, both ABX (i.g.) and ABX (i.v.) treatments eliminated tumor-resident bacteria (Fig. 3e), which is consistent with the 16S rRNA sequencing results. LEfSe analysis shows that VSVΔ51 treatment increased the richness of lots of bacteria in feces, such as *Alistipes, Barnsiella, Clostridium_XIVa, Clostridium_IV, Rikenella*, and *Acetatifactor*. Importantly, *Lactobacillus* was significantly decreased after VSVΔ51 treatment (Fig. 3f and Supplementary Fig. 2e). Meanwhile, lots of liver cancer tissue-resident bacteria were increased after VSVΔ51 treatment, such as *Barnsiella, Bacteroides, Oscillospira, Allobaculum, Clostridium_XIVa, Coprococcus, Alistipes* and *Oscillibacter*. Abundance of *Robinsoniella* was decreased after VSVΔ51 treatment (Fig. 3g and Supplementary Fig. 2f). Together, these data suggest that VSVΔ51 treatment can affect the composition of both gut and tissue-resident microbiota.

With these different antibiotic treatment strategies, we next aimed to address the role of gut microbiota and tumor-resident microbiota in oncolytic virotherapy. The results show that: (i) i.v. (ABX) treatment and i.g. (ABX) treatment can both enhance the oncolytic effect of VSVΔ51; (ii) i.g. (ABX) treatment enhanced antitumor effects of VSVΔ51 is better than i.v. (ABX) treatment (Fig. 3h); (iii) i.g. (ABX) treatment significantly induces smaller tumor size, better mice survival, increased infiltration of DCs ($F4/80^-$ $MHCII^+$ $CD11c^+$) and cytotoxic $CD8^+$ T cells (Granzyme B^+, TNF-α^+, and IFN-γ^+), decreased infiltration of regulatory T cells ($CD25^+$ $FOXP3^+$) and exhausted $CD8^+$ T cells ($TIGIT^+$), as well as decreased Ki-67 staining and increased cleaved-Caspase-3 staining when compared with i.v. (ABX) during VSVΔ51 oncolytic virotherapy (Fig. 3i and Supplementary Fig. 2g-2i). These data collectively demonstrate that gut microbiota plays a much crucial role in compromising the antitumor effect of VSVΔ51 when compared with the tumor-resident microbiota.

Strain-by-strain profiling shows that specific bacteria strains mitigate VSVΔ51 antitumor effect

Next, we sought to examine which strain can modulate OVs' antitumor effect. We designed a co-culture screen in which HuH7 cell line was co-cultured with bacterial strains from 10 phylum (27 bacterial strains) that were regulated by VSVΔ51 in vivo (refer to Fig. 2l). (i) Tumor cell viability was assessed after treatment with increasing multiplicity of infection (MOI) of VSVΔ51 plus various bacterial strains. EC_{50} (median effect dose) shift and differences in the area under the curve (DAUCs) for each bacterial strain were calculated. (ii) Viral fluorescence intensity (GFP, flow cytometry) and (iii) mRNA levels (qPCR) were applied to identify intracellular viral content. (iv) $TCID_{50}$ was performed to detect the secreted viral particles (Fig. 4a).

Remarkably, the results show that most bacteria upregulated by VSVΔ51 can attenuate the oncolytic efficacy (defined as DAUC < -0.3, bacteria strain ratio: 13/27) (Fig. 4b and Supplementary Fig. 3). These bacteria characterized are *Alistipes strains, Rikennella microfusus, Klebsiella oxytoc, Ligilactobacillus animals, Lactobacillus salivarius strain, Lactobacillus fermentum, Clostridium methylpentosum, Clostridium scindens, Clostridium boltei* and *Blautia hansenii*. Accordingly, intracellular viral loading and secreted viral particles were also decreased. By contrast, *Barnesiella intestinihominis* and *Lactobacillus apodemi* can enhance OVs' antitumor effect (defined as DAUC > 0.3, bacteria strain ratio: 2/27) (Supplementary Fig. 3), with concurrent elevation of viral replication. The other bacteria have no impact on antitumor effect of OVs (defined as -0.3 < DAUC < 0.3, bacteria strain ratio: 12/27) (Fig. 4b and Supplementary Fig. 3). We observed that DAUC is positively correlated with viral mRNA, viral GFP and viral titer, suggesting that bacteria-mediated oncolytic effect regulation is dependent on viral replication (Fig. 4c). On the basis of the study, we found that most of the strains analyzed can limit the oncolytic effect. Together, these data strongly demonstrate that based on bacteria strain profiling, most bacteria strains can mitigate oncolytic virotherapy while few bacterial strains are posing effect to enhance oncolytic virotherapy.

L. acidophilus supplementation boosts up the antitumor efficacy of oncolytic virothrapies

Given that lots of bacteria attenuated the antitumor effect of VSVΔ51 in oncolytic virotherapy assay, we wondered whether

https://doi.org/10.1038/s41467-025-58407-z

potential probiotics could enhance oncolytic virotherapy through harnessing microbiota homeostasis[32]. Microbial profiling reveals that *Lactobacillus* is negatively correlated with lots of bacteria, including *Barnsiella, Blautia, Clostridium_XIVa, Akkermansia, Desulfovibrio, Acetatifactor, Clostridium_IV, Alistipes* and *Rikenella* (Fig. 5a). Furhter searching probiotics from *Lactobacillus* genus, we found that *Lactobacillus acidophilus* (*L. acidophilus*) is one of the most widely used probiotics owing to its regulating role of the balance of intestinal flora[33,34]. FISH assay revealed that VSVΔ51 treatment increases total bacteria abundance while reduces *L. acidophilus* abundance in mouse intestines (Fig. 5b). This observation led us to hypothesize whether *L. acidophilus* supplementation

Fig. 2 | VSVΔ51 treatment modulates gut homeostasis, changing gut transit time, metabolome, and microbiota composition. a Schematic of the experimental design. Created in BioRender. Yang, X. (2025) https://BioRender.com/r48z536. **b** Fecal output and water content in feces were shown ($n = 4$/group). **c** Small intestine transit (%) and whole gut transit time were shown ($n = 4$/group). **d** Score plot presenting the metabolic separation for pair splitting between groups through oPLS-DA ($n = 4$/group). **e** Volcano plot showing the differential metabolites in the comparison of VSVΔ51 to control. **f** Overview of the top 20 terms in the metabolic enrichment analysis of the differential metabolites. **g** Unsupervised PCoA clustering analysis of the feces bacteria using unifrac distance. MRPP test *P*-value is 0.0001. **h** Alpha-diversity Chao1 index of 16S sequencing data ($n = 9$ for ABX; $n = 10$ for other groups). Data are presented as box plots (center line at the median, upper and lower bounds are 75th and 25th percentile with whisker at 1.5 IQR). **i** Stacked bar plot showing the bacteria relative abundance at the phylum and genus level in various samples ($n = 9$ for ABX; $n = 10$ for other groups). **j**, **k** Proportional Chord Diagram showing the top-ranked significantly changed bacteria in two repeated experiments. **l**, **m** LEfSe analysis showed differences in bacterial profiles among the two groups ($n = 9$–10/group) in two repeated experiments. **b**, **c** Unpaired, two-tailed Student's *t*-test. **e**, **f** One-tailed Student's *t*-test. **h** One-way ANOVA with Tukey post-hoc test were used. Results are presented as mean ± S.D. Each spot represents one subject. Source data are provided in the Source Data file.

can reprogram the gut microbiota homeostasis and enhance oncolytic effect of VSVΔ51.

As previous report shows that either alive or heat inactivated probiotics can regulate gut microbiota composition[35], we next tested that if pre-heated *L. acidophilus* and/or alive *L. acidophilus* could enhance antitumor efficacy of VSVΔ51. Tumor bearing mice (C57 mice were subcutaneously injected H22 cell line) were treated with (i) control, (ii) *L. acidophilus*, (iii) VSVΔ51, (iv) *L. acidophilus* + VSVΔ51, (v) *L. acidophilus* (pre-heated) and (vi) *L. acidophilus* (pre-heated) + VSVΔ51. The results showed that mice treated with *L. acidophilus* + VSVΔ51 or *L. acidophilus* (pre-heated) + VSVΔ51 had significant slower tumor growth (Fig. 5c) when compared with other groups, suggesting that either alive or pre-heated *L. acidophilus* can significantly enhance the antitumor efficacy of VSVΔ51-mediated oncolytic virotherapy. At the same time, all of the treatment does not affect mice weight (Fig. 5d). From tumor size observation at the end point, we observed that alive *L. acidophilus* + VSVΔ51 and *L. acidophilus* (pre-heated) + VSVΔ51 had smallest tumor size compared with other group (Fig. 5e, f). However, the antitumor effect of alive *L. acidophilus* + VSVΔ51 is better than *L. acidophilus* (pre-heated) + VSVΔ51.

Next, we wondered whether harnessing micriobiota could affect the antitumor effect of other classical oncolytic viruses, tumor bearing mice were treated with HSV-1 armed with anti-PD-1 antibody or VACV(WR)-GFP with or without *L. acidophilus*. Our results shows that *L. acidophilus* could significantly enhance antitumor efficacy of HSV-1-anti-PD-1 or VACV(WR)-GFP, as evidenced by decreased tumor growth curve, reduced tumor size and without affecting the mice weight at the end point (Fig. 5g–n). These data strongly indicate that *L. acidophilus* supplementation could significantly enhance the antitumor effect of oncolytic viruses.

L. acidophilus supplementation facilitates antitumor immune response of VSVΔ51 through reprogramming microbiome

Next, we asked whether enhanced oncolytic virotherapy by *L. acidophilus* is dependent on the existence of gut microbiota. We established two HCC mice models, H22 cell line intra-liver injection orthotopic model and a hydrodynamic tail vein injection (HDTI) genetic HCC mice model. HA-*myr-Akt*, N90-*β-catenin*, and *Sleeping Beauty* (SB) transposon constructs were delivered into the liver of C57 mice by hydrodynamic tail vein injection to establish HCC model[36,37]. Mice were treated with (i) control, (ii) *L. acidophilus*, (iii) VSVΔ51, (iv) *L. acidophilus* + VSVΔ51 in the presence or absence of antibiotics (Supplementary Fig. 4a).

The results showed that in the presence of microbiota (-ABX), mice treated with the *L. acidophilus* + VSVΔ51 combination had the smallest tumor area and prolonged survival when compared with other groups in both H22 orthotopic model and HDTI model (Fig. 6a–c). Strikingly, the combination group shows total tumor regression in HDTI model (Fig. 6d–f). The combination group had decreased tumor area as assayed by H&E staining, decreased Ki-67 level, and increased cleaved-Caspase-3 level (Supplementary Fig. 4b and 4c). Meanwhile, the combination group had increased cytotoxic $CD8^+$ T cells (TNF-α^+, IFN-γ^+ and Granzyme B^+) (Fig. 6g), decreased exhausted $CD8^+$ T cells, and decreased regulatory $CD4^+$ T cells ($CD25^+$ $FOXP3^+$) in the tumor microenvironment (Supplementary Fig. 4d). In the presence of ABX, the *L. acidophilus* + VSVΔ51 combination group was no different from VSVΔ51 group in terms of antitumor effect as evidenced by tumor area, mice survival, effector $CD8^+$ T cells, exhausted $CD8^+$ T cells and regulatory $CD4^+$ T cells (Fig. 6a–g, Supplementary Fig. 4b–d).

Moreover, through 16S rRNA sequencing, *L. acidophilus* supplementation in VSVΔ51-treated mice changes microbiota composition when compared with VSVΔ51-treated mice as demonstrated by PCoA analysis and alpha diversity analysis (Fig. 6h, i). Strikingly, *L. acidophilus* supplementation in VSVΔ51-treated mice diminished the abundance of bacteria upregulated by VSVΔ51-treated mice, including *Alistipes*, *Acetatifactor*, *Rikenella*, *Clostridium_IV* and *Clostridium_XIVa* (Fig. 6j). RNA sequencing and Gene Set Enrichment Analysis (GSEA) analyses from VSVΔ51-treated mouse gut epithelial tissues were performed. We found that cell adhesion-related pathways were enriched in VSVΔ51-treated mice group based on KEGG analysis and Gene Ontology analysis (Supplementary Fig. 5a-5d). VSVΔ51-treated mice markedly decreased the expression of tight junction mRNA, including *Tjp1* (ZO-1), *Ocln* (Occludin), and *Cdh1* (E-cadherin) (Supplementary Fig. 5e). *L. acidophilus* supplementation in VSVΔ51-treated mice restores the gene expression of these three genes downregulated by VSVΔ51 (Supplementary Fig. 5e). Accordingly, Occludin1 and E-cadherin expression diminished by VSVΔ51 was rescued by *L. acidophilus* supplementation in VSVΔ51-treated mice (Supplementary Fig. 5f). Detailed assessment using transmission electron microscopy (TEM) demonstrated that *L. acidophilus* supplementation in VSVΔ51-treated mice restored the fragmented/destroyed cell-cell junction caused by VSVΔ51 (Supplementary Fig. 5g). Taken together, these data indicate that *L. acidophilus* reduced by VSVΔ51 might lead to the deregulation of gut barrier (tight junction) function and alteration of microbiota composition, thereby compromising the efficacy of oncolytic virotherapy. Supplementation of *L. acidophilus* can strengthen oncolytic virotherapy efficacy of VSVΔ51 through modulating microbiota composition and restore gut barrier function.

VSVΔ51 downregulates SLC20A1 via IL-6-STAT3 axis to reduce the attachment of *L. acidophilus* to intestinal tissue and subsequent gut colonization

To investigate how VSVΔ51 reduces *L. acidophilus* colonization in the intestine, we collected mice epithelial tissues after VSVΔ51 treatment and performed RNA-sequencing (RNA-seq). Meanwhile, we performed biotinylated *L. acidophilus* pull-down assay to characterize *L. acidophilus* interacting epithelial proteins by mass spectrometry[38,39]. Based on the identification of the candidate *L. acidophilus*-interacting proteins (including membrane proteins) and characterization of VSVΔ51-mediated downregulated genes (including membrane genes) by RNA-seq, we revealed one major membrane protein SLC20A1 could be the candidate membrane protein interacting with *L. acidophilus* and was downregulated by VSVΔ51 (Fig. 7a, Supplementary Fig. 6a, b). Far-Western results showed that a potential *L. acidophilus* -interacting protein near 75 kDa (SLC20A1) was decreased after VSVΔ51 treatment (Fig. 7b).

https://doi.org/10.1038/s41467-025-58407-z

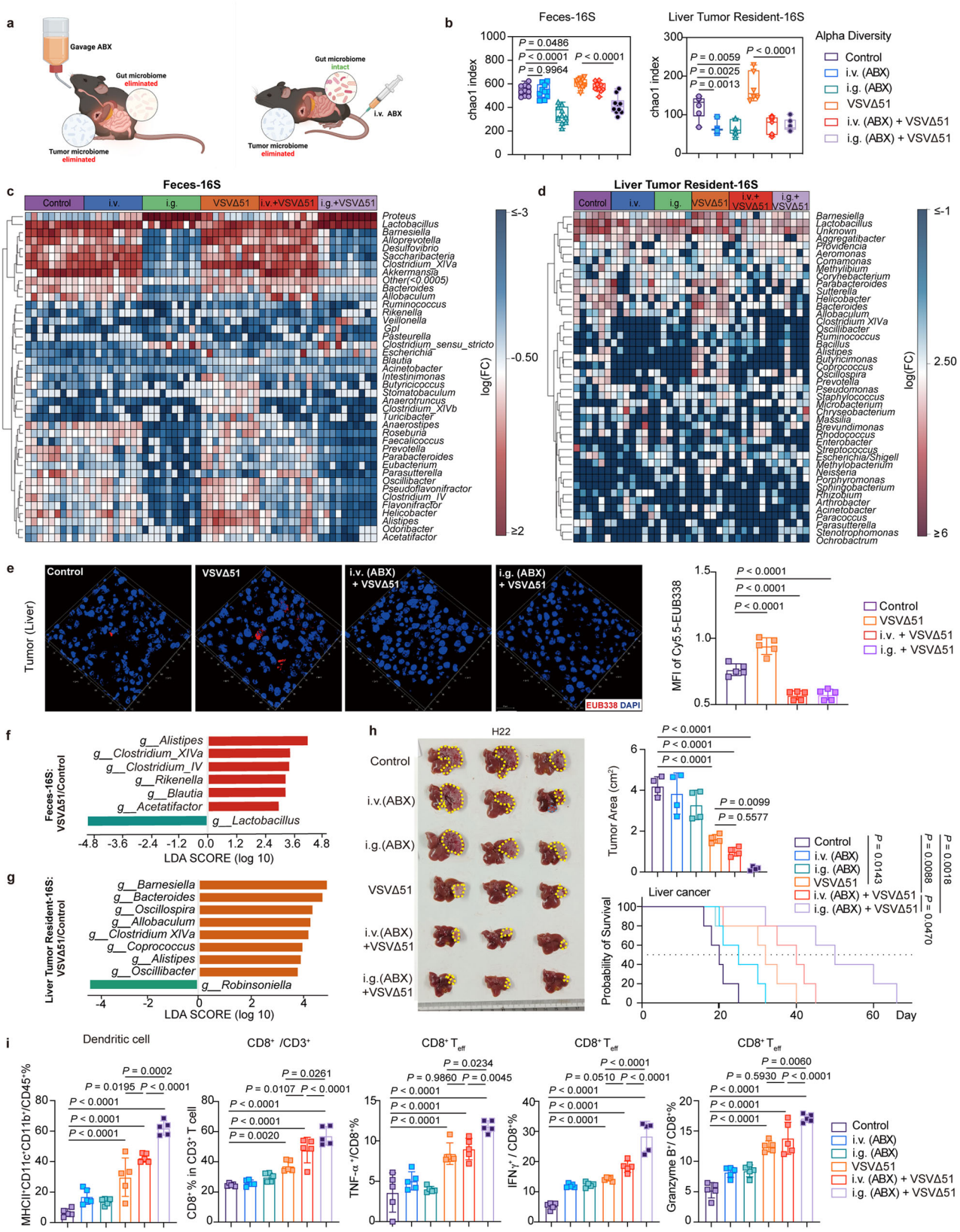

To address the role of SLC20A1 on *L. acidophilus* colonization, we found that Dox-induced knockdown of SLC20A1 attenuated the attachment of *L. acidophilus* to NCM460 cell, an intestinal epithelial cell line, based on colony formation assay (Fig. 7c and Supplementary Fig. 6c). Of note, SLC20A1 KD does not affect the cell viability (Supplementary Fig. 6d and 6e). Significantly, we observed that the attachment of *L. acidophilus* to NCM460 cell was indeed compromised when SLC20A1 gene was knocked down in NCM460 cells based on TEM, immunofluorescence, and scanning electron microscope (SEM) studies (Fig. 7d-f). Membrane protein topology analysis shows that SLC20A1 is a sodium-dependent phosphate transporter with 5 outside membrane domains[40] (Fig. 7g). We demonstrated that the second

https://doi.org/10.1038/s41467-025-58407-z

Fig. 3 | The presence of gut microbiome compromises the antitumor effect of VSVΔ51. a Schematic diagram showing administration strategies of antibiotics and the influences on the gut and tissue microbiota. Created in BioRender. Yang, X. (2025) https://BioRender.com/q52l414. **b** Alpha-diversity Chao1 index of feces ($n = 10$/group) and liver tumor-resident bacteria ($n = 6$ for control, i.g., VSVΔ51 and i.g. + VSVΔ51, $n = 7$ for other groups). Data are presented as box plots (center line at the median, upper and lower bounds are 75th and 25th percentile with whisker at 1.5 IQR). **c**, **d** Heatmap representation of differentially abundant bacterial species in feces and liver tumor. **e** 16S FISH analysis of orthotopic tumor. Red, 16S FISH probe. Blue, DAPI. Scale bar, 20 μm (n = 5/group). **f**, **g** LEfSe analysis showing differences in bacterial profiles among feces and liver tumor between the two groups. **h** Representative images of tumor from each group were shown ($n = 4$/group). Dashed yellow lines represent tumor areas and the areas were calculated. Kaplan-Meier survival curves were shown ($n = 5$/group). **i** At the end of the experiment, the mice were sacrificed, and immune cells from TME were analyzed by flow cytometry. Statistical data for the proportion of dendritic cells, $CD8^+$ T cells, Granzyme B^+ cells, IFN-γ^+ cells and TNF-α^+ cells among live cells in the TME were presented ($n = 5$/group). **b**–**i** One-way ANOVA with Tukey post-hoc test were used, Kaplan-Meier survival curves, and statistical differences between curves were analyzed using the log-rank test. Results are presented as mean ± S.D. Each spot represents one subject. Source data are provided in the Source Data file. See also Supplementary Fig. 2.

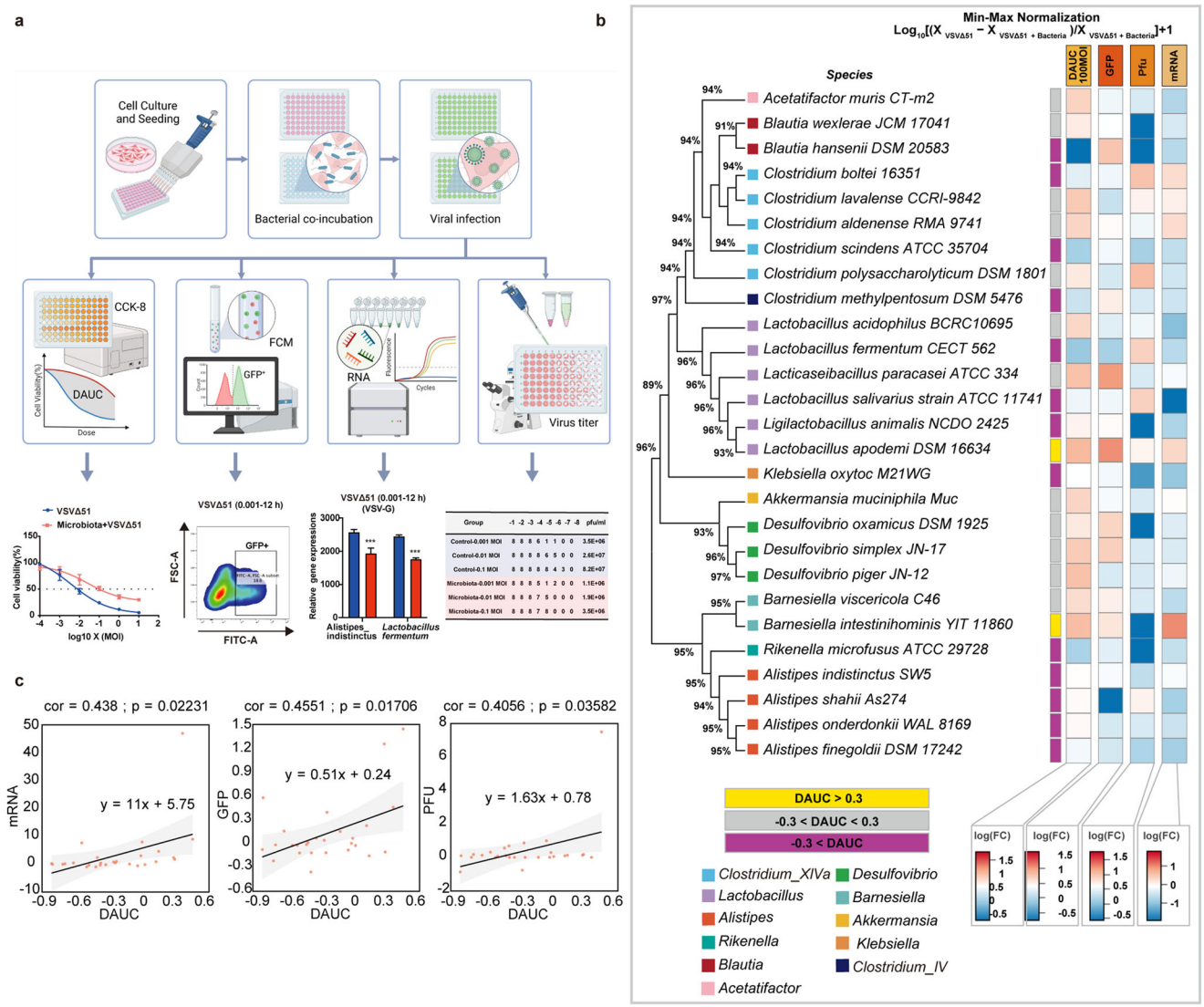

Fig. 4 | Oncolytic virotherapy-regulated bacteria can mitigate VSVΔ51 antitumor effect. a An outline of bacteria screening protocol. HuH7 cells were treated with increasing MOI of VSVΔ51 with or without bacterium from the community. Cell viability (at VSVΔ51 for 48 h), viral GFP, viral RNA (VSV-G) and viral titer (at VSVΔ51 for 12 h) were determined. The DAUC was calculated according to the following formula: $(AUC_{VSV\Delta51} - AUC_{VSV\Delta51 + Bacteria})/AUC_{VSV\Delta51 + Bacteria}$; FCM, Flow Cytometry. Created in BioRender. Yang, X. (2025) https://BioRender.com/j49g663. **b** Phylogenetic tree of Bacteria and the screening results were shown. **c** Correlation analysis of DAUCs with viral mRNA (95% CI = [0.0000, 0.8760]), viral GFP (95% CI = [0.2784, 0.6318]) or titer (95% CI = [0.0000, 0.8120]), used Pearson correlation coefficient. Source data are provided in the Source Data file. See also Supplementary Fig. 3.

domain (78-158 amino acids, aa) of SLC20A1 is critical for *L. acidophilus* binding based on a domain mapping experiment (Fig. 7h). We demonstrated that the attachment of *L. acidophilus* to NCM460 cell transfected with SLC20A1Δ2 was decreased when compared with wildtype (WT) SLC20A1 (Fig. 7i). Several proteins of *L. acidophilus* that can interact with SLC20A1 were characterized by immunoprecipitation-mass spectrometry (IP-MS) including a cell wall protein CdpA (Fig. 7j). CdpA is the candidate that binds strongly with SLC20A1 among other possible candidates (Fig. 7k and Supplementary Fig. 6f). Moreover, the binding between SLC20A1 with CdpA depends

https://doi.org/10.1038/s41467-025-58407-z

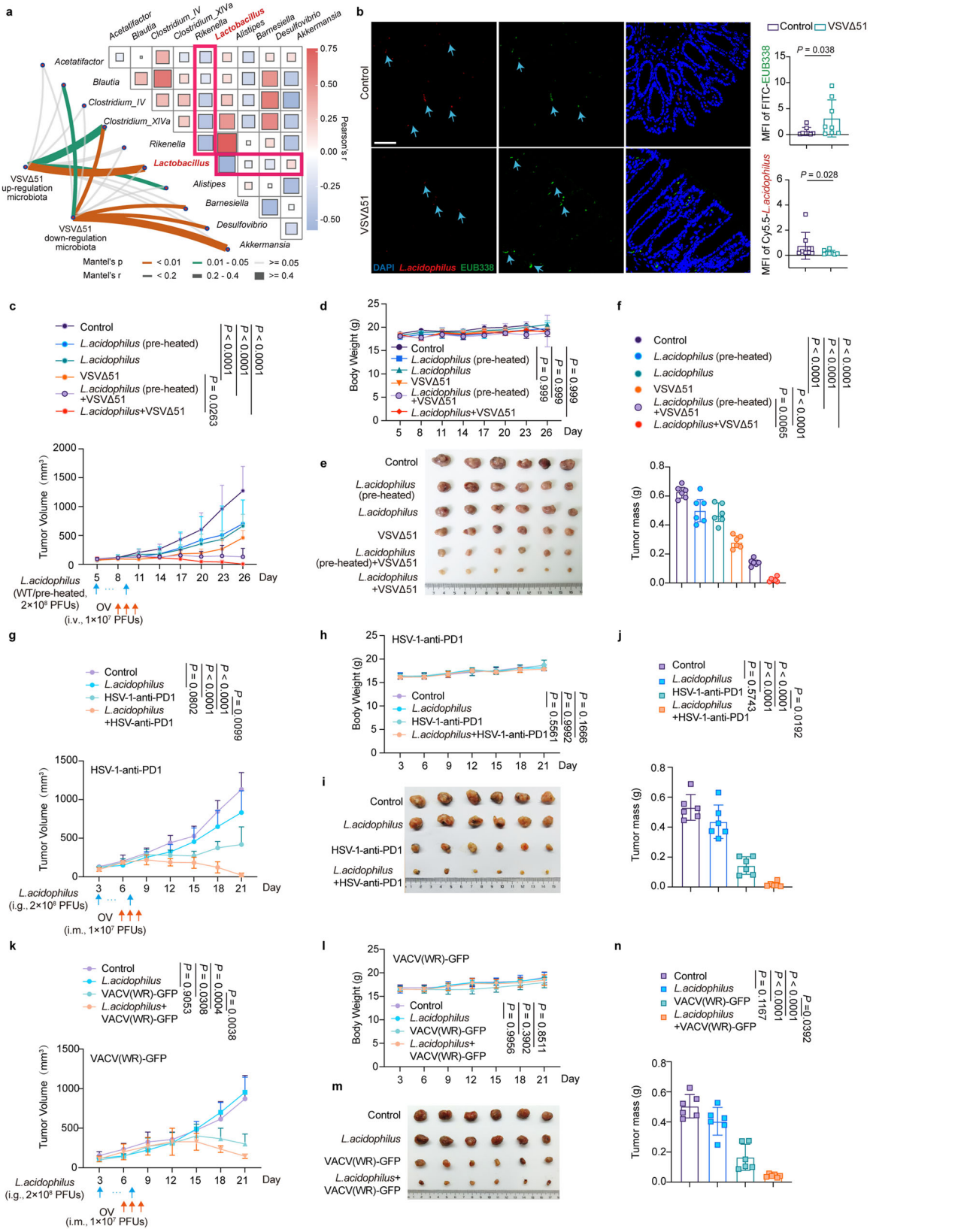

on the second domain of SLC20A1 as SLC20A1Δ2 reduces its binding to CdpA (Fig. 7l). The binding between SLC20A1 second domain (78-158 aa) and CdpA was modeled using PyMOL program[41] (Fig. 7m). These observations suggest that SLC20A1 of intestinal cells, which binds cell wall protein CdpA of *L. acidophilus*, is crucial for *L. acidophilus* attachment and subsequent gut colonization.

SLC20A1 was identified during intestine tissue RNA sequencing screening. To determine the mechanism behind which VSVΔ51 down-regulates SLC20A1 expression, we first examine *SLC20A1* mRNA and protein levels of NCM460 cells infected with VSVΔ51 in a dose-dependent manner. Surprisingly, VSVΔ51 treatment does not down-regulate *SLC20A1* mRNA and protein levels in NCM460 cell context

Fig. 5 | *L. acidophilus* supplementation enhances oncolytic effect of oncolytic virohterapy. a Mantel test analysis of the correlations between the VSVΔ51 up-regulated and down-regulated microbiota. *L. acidophilus* negatively correlates with other bacteria (Highlighted with red line). **b** The colonic abundance of *L. acidophilus* as determined by FISH. 16S was stained with green fluorescence (EUB338) and *L. acidophilus* was stained with red fluorescence (specific probe) (n = 8/group). **c** H22 cells were subcutaneously injected into C57 mice, VSVΔ51 were intravenously administrated (1×10^7 PFUs, i.v., 3 times) after *L. acidophilus* or *L. acidophilus* (per-heated) (2×10^8 PFUs, i.g., total 5 times) treatment 4 times. Tumor growth was measured ($n = 6$/group). **d** Mice body weight were shown ($n = 6$/group). **e**, **f** Gross tumor and tumor mass were shown ($n = 6$/group). **g** H22 cells were subcutaneously injected into C57 mice, HSV-1-anti-PD1 were intratumoral (i.m.) administrated (1×10^7 PFUs, i.m., 3 times) after *L. acidophilus* (2×10^8 PFUs, i.g., total 5 times) treatment 4 times. Tumor growth was measured ($n = 6$/group). **h** Mice body weight were shown ($n = 6$/group). **i**, **j** Gross tumor and tumor mass were shown ($n = 6$/group). **k** H22 cells were subcutaneously injected into C57 mice, VACV(WR)-GFP were Intratumoral administrated (1×10^7 PFUs, i.m., 3 times) after *L. acidophilus* (2×10^8 PFUs, i.g., total 5 times) treatment 4 times. Tumor growth was measured ($n = 6$/group). Tumor growth was measured ($n = 6$/group). **l** Mice body weight were shown ($n = 6$/group). (**m** and **n**) Gross tumor and tumor mass were shown ($n = 6$/group). (**b**) Unpaired, two-tailed Student's *t*-test. **c**–**l** Two-way ANOVA. **f**–**n** One-way ANOVA with Tukey post-hoc test. Results are presented as mean ± S.D. Each spot represents one subject. Source data are provided in the Source Data file.

(Supplementary Fig. 6g, h). By contrast, we confirmed that VSVΔ51 treatment indeed decrease the *Slc20a1* expression in intestinal tissues context as evident by qPCR and Western blot (Supplementary Fig. 6i, j). In addition to direct tumor-killing, OVs (VSVΔ51) are well-known to induce bystander killing through cytokine storms[42,43]. Thus, the seemingly contradictory data in different context led us to hypothesize that *Slc20a1* expression might be regulated by circulating inflammatory factors.

To this end, cytokines array was performed using serum from VSVΔ51-treated mice. As the data show, IL-12p40, G-CSF, IL-6 and IL-10 were significantly decreased after VSVΔ51 treatment (Supplementary Fig. 6k). Importantly, exogenous addition of these inflammatory factors, including IL-6, to cells could upregulate SLC20A1 expression (Supplementary Fig. 6l). Interestingly, IL-6, G-CSF, IL-12B and IL-10 are upstream of STAT3 signaling[44–46]. We found that IL-6-mediated upregulation of SLC20A1 can be blocked with JAK-1/2-STAT3 inhibitor Ruxolitinib, suggesting that IL-6-STAT3 axis is involved in regulating SLC20A1 expression (Supplementary Fig. 6m). Indeed, *SLC20A1* promoter has STAT3-binding motif based on JASPAR program analysis[47] (Supplementary Fig. 6n). Chromatin immunoprecipitation (ChIP) assay confirmed that *IL-6* signaling enhances binding of *phosphorylated-STAT3* and RNA polymerase 2 (*Pol2*) to the *SLC20A1* promoters, suggesting the transcriptional activation of *SLC20A1* by *IL-6-STAT3* axis (Supplementary Fig. 6n). Together, these results demonstrated that VSVΔ51-mediated downregulation of IL-6 attenuates STAT3 signaling, thereby reducing the expression of SLC20A1 and subsequent loss of *L. acidophilus* attachment (colonization) to intestinal cells. In summary, the oncolytic virotherapy elicits host responses, which shapes microbiome populations and inhibits viral replication. VSVΔ51 infection caused downregulation of *IL-6*, which leads to repression of *SLC20A1* gene expression through blocking *STAT3* signaling. Thus, *L. acidophilus* attachment to SLC20A1 and subsequent colonization in gut tissue decreased, thereby reshaping the landscape of microbiota in the gut (Supplementary Fig. 7).

Discussion

Hepatocellular carcinoma, presenting a very dismal prognosis, is usually resistant to conventional chemotherapy and radiotherapy. Oncolytic virotherapy has been explored in HCC. Despite increasing interest of oncolytic virotherapy, the underlying biology and pharmacology of OVs are not fully understood. A better understanding regarding these issues is needed to fully employ therapeutic potential of OVs in cancer patients. We demonstrate that the existence of microbiota might be a prominent factor impacting oncolytic virotherapy.

Microbiota influence the efficacy of VSVΔ51-mediated oncolytic virotherapy

Studies show that microbial signals are required in the development of cancer, which is reminiscent of the observation that hematopoietic malignancies were compromised by antibiotic treatment and also failed to develop in germ-free mice[48]. Another similar observation is that germ-free condition or antibiotic-treatment significantly compromises lung cancer development in mice model[49]. Using antibiotic cocktail to abolish the microbiota composition can potentiate the efficacy of VSVΔ51 oncolytic virotherapy, suggesting that the existence of microbiota may be a hurdle for treatment. One can imagine that the presence of commensal bacteria (microbiota) can stimulate *Myd88*-dependent IL-1β and IL-23 production from myeloid cells, thereby activating T cells to produce IL-17/other effector molecules and promoting inflammation and tumor cell growth[49]. It is then clear that oncolytic virotherapy of VSVΔ51 encounters a barrier to preclinical effectiveness due to the presence of microbiota. Thus, tumor may become resistant, resulting in treatment failure. Indeed, we show that specific bacteria strains mitigate VSVΔ51 antitumor effect. This limitation of inducing complete tumor regression by VSVΔ51 has prompted us to explore the mechanism and new approaches targeting tumors that are resistant to oncolytic virotherapy of VSVΔ51.

Although we observed encouraging results in mice models, it should be noted that the composition of human microbiome is relatively different to mice microbiome. Gut microbiota plays an important role in liver homeostasis and HCC progression[50,51]. The further alteration of microbiome composition after oncolytic virotherapy in HCC patients and other cancer patients deserves further investigation. Moreover, patient-relevant models are also needed to confirm our observations in future studies. Although these concerns exist, the potential clinical implications of this research are noteworthy, as our study provides a clear rationale for complementing OVs with *L. acidophilus* for improvement of OVs applications in HCC therapy. *L. acidophilus* supplementation not only restores gut microbiome balance after VSVΔ51-induced dysbiosis but also improves gut barrier function and modulates host immunity, which collectively enhances the replication and efficacy of the OVs. In all, our results uncovered an unrecognized feature of OVs: microbiome alteration plays an important role in oncolytic virotherapy.

L. acidophilus improves barrier integrity disturbed by VSVΔ51

L. acidophilus is one of the most widely used and studied probiotics owing to its favorable safety profile and efficacy[52]. *L. acidophilus* exhibits important technical properties, i.e., thermostability and retaining of activity at a wide pH range along with strong inhibitory actions against food spoilage and pathogenic bacteria make them an important class of biopreservatives[53]. Many report shows that *L. acidophilus* can regulate the balance of intestinal flora by reducing the intestinal pH and producing metabolites[33,34].

During treatment, VSVΔ51 causes disturbances in the tightness of gut barrier (loss of Occludin and E-cadherin), possibly leading to the potential penetration of toxins/harmful bacterial products into the system, which leads to more systemic infections and inflammation, compromising oncolytic effect. It is not clear whether VSVΔ51-mediated elevation of TNF-α may lead to this intestinal barrier dysfunction. However, few VSVΔ51-reduced bacterial strains, such as *L. acidophilus*, are able to enhance VSVΔ51 oncolytic virotherapy. It is known that *L. acidophilus*-intestinal barrier

https://doi.org/10.1038/s41467-025-58407-z

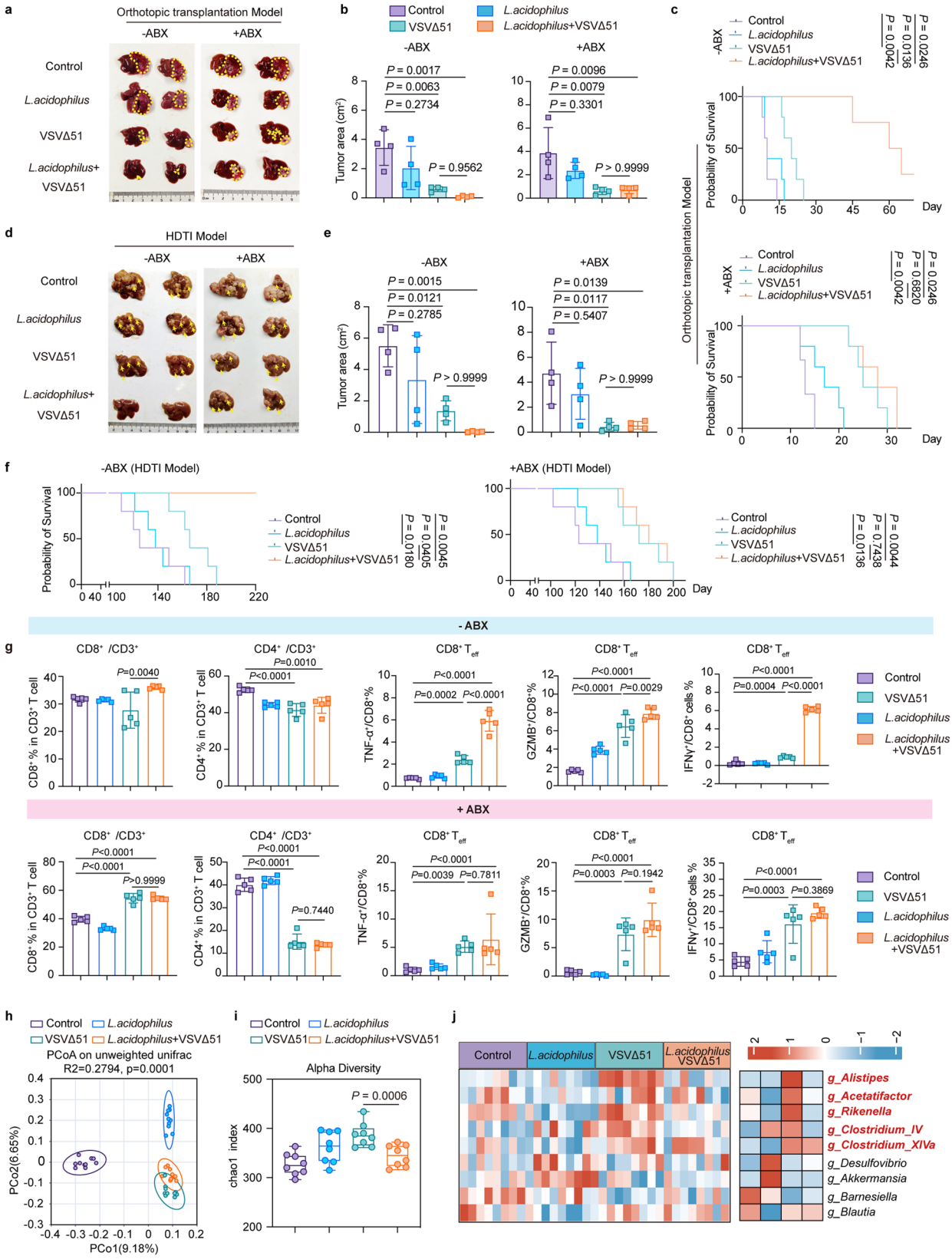

regulation can result in the prevention of gut-barrier defects although mechanisms are not well defined[54]. We found that *L. acidophilus* indeed ameliorates the disturbance of barrier integrity by restoring the expression of tight junction proteins such as Occludin and E-cadherin, with concurrently high efficacy of VSVΔ51 oncolytic virotherapy.

L. acidophilus attachment can boost up efficacy of VSVΔ51

Mechanistically, *L. acidophilus* binds SLC20A1/PiT1 of gut tissue for attachment. We show that VSVΔ51–mediated blocking of IL-6-STAT3 signaling is critical for SLC20A1 downregulation, thereby reducing *L. acidophilus* attachment to gut tissue. Significantly, *L. acidophilus* in combination with VSVΔ51 improves therapeutic outcomes. We find

Fig. 6 | *L. acidophilus* supplementation enhances antitumor immune response of VSVΔ51 via changing the landscape of microbiota. a Orthotopic mice models were established (H22 cell line). Representative images of tumor from each group were shown ($n = 2$/group). **b** Dashed yellow lines represent tumor areas and the areas were calculated ($n = 4$). **c** Kaplan-Meier survival curves were shown ($n = 5$/group). **d** Orthotopic mice models were established (spontaneous HCC by HDTI). Representative images of tumor from each group were shown ($n = 2$/group). **e** Dashed yellow arrow represent tumor areas and the areas were calculated ($n = 4$/group). **f** Kaplan-Meier survival curves were shown ($n = 5$/group). **g** At the end of the experiment, the mice were sacrificed, and immune cells from TME were analyzed by flow cytometry. Statistical data for the proportion of $CD8^+$ T cells among $CD3^+$ T cells, $CD4^+$ T cells ($CD3^+$ $CD4^+$), Granzyme B^+ cells ($CD3^+$ $CD8^+$ $GZMB^+$), IFN-γ^+ ($CD3^+$ $CD8^+$ IFN-γ^+), TNF-α^+ ($CD3^+$ $CD8^+$ TNF-α^+) were shown ($n = 5$/group). **h** Unsupervised PCoA clustering analysis of the HDTI mice (without ABX treatment) feces bacteria using unifrac distance. MRPP test p-value is 0.0001($n = 9$/group). **i** Alpha Diversity analysis was shown. Data are presented as box plots (center line at the median, upper and lower bounds are 75th and 25th percentile with whisker at 1.5 IQR). **j** Heatmap showing differentially abundant bacterial species in mice. **b**–**i** One-way ANOVA with Tukey post-hoc test. **c**, **f** Kaplan-Meier survival curves, and statistical differences between curves were analyzed using the log-rank test. Results are presented as mean ± S.D. Each spot represents one subject. Source data are provided in the Source Data file. See also Supplementary Figs. 4 and 5.

that *L. acidophilus* improves barrier integrity, increases cytotoxic $CD8^+$ T cells, and decreases exhausted $CD8^+$ T cells in the tumor microenvironment; therefore, providing preclinical proof-of-principle for enhancing oncolytic virotherapy in liver cancer.

SLC20A1/PiT1 protein is a Na (+)-dependent cotransporters for transporting phosphate across cell membranes, involving in maintaining Pi homeostasis. It is shown that SLC20A1/PiT1-depleted cells are more sensitive to the proapoptotic activity of TNF-α[55]. Thus, VSVΔ51-mediated down regulation of SLC20A1/PiT1 may also facilitate TNF-α-mediated cell apoptosis. Although SLC20A1 transporter is characterized as a receptor of *L. acidophilus*, it remains to be determined whether *L. acidophilus* can act through SLC20A1 transporter to potentiate some signaling pathways, such as TNF-α, for enhancing the efficacy of VSVΔ51. *L. acidophilus* attachment to the sites on the gut epithelium may also be affected by the VSVΔ51-mediated elevation of other symbionts, which may also directly antagonize *L. acidophilus* through contact-dependent inhibition, the type VI secretion system (T6SS) or secreted molecules such as bacteriocins[56–59]. However, these issues warrant further investigation. As for the *L. acidophilus* CdpA protein that interacts with SLC20A1, it is not clear that *L. acidophilus* CdpA has any other functions other than attachment. Whether it uses its cyclic di-GMP phosphodiesterase activity for regulating host functions warrants further investigation. For example, Burkholderia pseudomallei CdpA is characterized to be involved in auto aggregation, flagellum synthesis, motility, biofilm formation, cell invasion, and cytotoxicity[60].

Taken together, these studies enable the potential development of employing combination of microbiota modifier that reprograms the tumor microenvironment, triggering better anti-tumor immune responses to enhance the efficacy of oncolytic virotherapy and opens a great avenue for future medical practice.

Methods

Mouse models

Mouse experiments. Germ-free (GF) C57BL/6 J mice were bred and housed at the Shenzhen Gnotobio Biotechnology Co., Ltd. GF status was confirmed through 16S qPCR analysis before used for relative experiments, which were also carried out at Shenzhen Gnotobio Biotechnology Co., Ltd.

Conventionally housed 6-week-old C57BL/6 J wild-type mice were purchased from Guangdong GemPharmatech Co., Ltd, GUANGDONG MEDICAL LABORATORY ANIMAL CENTER and Sun Yat-sen University. Mice were fed with normal diet (PicoLab 5053, Purina) and maintained on a 12 h light/dark cycle (6 a.m–6 p.m.). Studies involving animals were approved by the Animal Ethical and Welfare Committee of Sun Yat-sen University (SYSU-IACUC-2023-002133) and Shenzhen Gnotobio Biotechnology (JTAW20240806-1, JTAW20241106-1 and JTAW20240605-1) and were carried out in accordance with the approved protocols.

Measurement of fecal output, water content, whole gut transit time and small intestinal transit. The fecal output was recorded for 3 h to detect the gut motility of mice. Each mouse's average number of fecal pellets per hour was measured for inter-individual comparisons. Fresh fecal pellets from each mouse were collected in a separate sterile EP tube. After calculating the wet weight, each sample was subject to a freeze dryer for 24 h to get the dry weight. The water content was calculated as the difference between the wet and dry weight of the representative fecal pellet. For whole gut transit time, mice were fasted overnight and were given an oral gavage of 250 µL of black ink. The mice were immediately transferred to a new, clean, empty individual cage. The whole gut transit or defecation time was calculated as the time required to defecate the first black stool pallet. For small intestinal transit, gastrointestinal motility was measured according to a previous report[61]. Briefly, mice were fasted overnight and were given an oral gavage of 250 µL of black ink. After 10 min, the abdomen of each mouse was opened, and the entire small intestine (from the pylorus to the cecum) was carefully taken out. The distance moved by ink and the total length of the small intestine were measured.

HCC mouse models. Hydrodynamic tail vein injection (HDTI) was performed based on the previous report[62]. HA-*myr-AKT*, N90-*β-catenin*, *Sleeping Beauty* (SB) and sg*Clock*/*Vector* were injected in 2 mL PBS within 7 s. For orthotropic mice model, H22 cells (50 µL, ~1×10^6 cells) were collected in PBS and intra-liver injected into 6-week-old female C57BL/6 J mice. The organs or tissues of each mouse were dissected and then fixed in 4% formaldehyde and embedded in paraffin. For subcutaneous mice model, H22 and Hepa 1–6 (1×10^6 cells per mouse) cells were inoculated subcutaneously into the hind-flanks of 6-week-old female C57BL/6 J mice. Tumor length and width were measured, and the volume was calculated according to the formula (length × width^2)/2. According to the Animal Ethics and Welfare Committee, the maximum tumor load allowed by the ethics committee was 1500 mm^3. The humane end point was when the tumor volume reached 1500 mm^3. For subcutaneous mice model, VSVΔ51 were intravenously administrated (1×10^7 PFUs) 3 times after *L. acidophilus* or *L. acidophilus* (per-heated) 3 times (2×10^8 PFUs, i.g., total 5 times). HSV-1-anti-PD1 and VACV(WR)-GFP administered by intratumoral injection (1×10^7 PFUs).

T/C% defined as the relative tumor proliferation rate, and T/C% values of <40% are considered to indicate an effective response. The T/C% was calculated as follows: $T/C\% = T_{RTV}/C_{RTV}$ 100%; V_t, tumor volume after treatment; V_0, tumor volume before treatment; RTV, relative tumor volume, $RTV = V_t/V_0$; T_{RTV}, RTV in the treatment group; C_{RTV}, RTV in the control group. At the end of experiments, tumor mass was calculated and tumor tissues were dissected and fixed in 4% formaldehyde.

Fecal microbiota transplantation (FMT)

Orthotropic mice model with H22 cells were established. Feces from mice treated with VSVΔ51 (tail vein injection) or not were collected and resuspended in PBS at a concentration of 0.125 g mL^{-1}. Mice were pretreated with antibiotics (ABX (500 µL each mouse), containing vancomycin (50 mg mL^{-1}; V105495, Aladdin, China), imipenem/cilastatin (25 mg mL^{-1}; C304719, I304258, Aladdin, China), neomycin (10 mg mL^{-1}; N412785, Aladdin, China), and amphotericin (1 mg mL^{-1}; A105482, Aladdin, China)) for 5 times. After administration of 0.15 mL fecal

https://doi.org/10.1038/s41467-025-58407-z

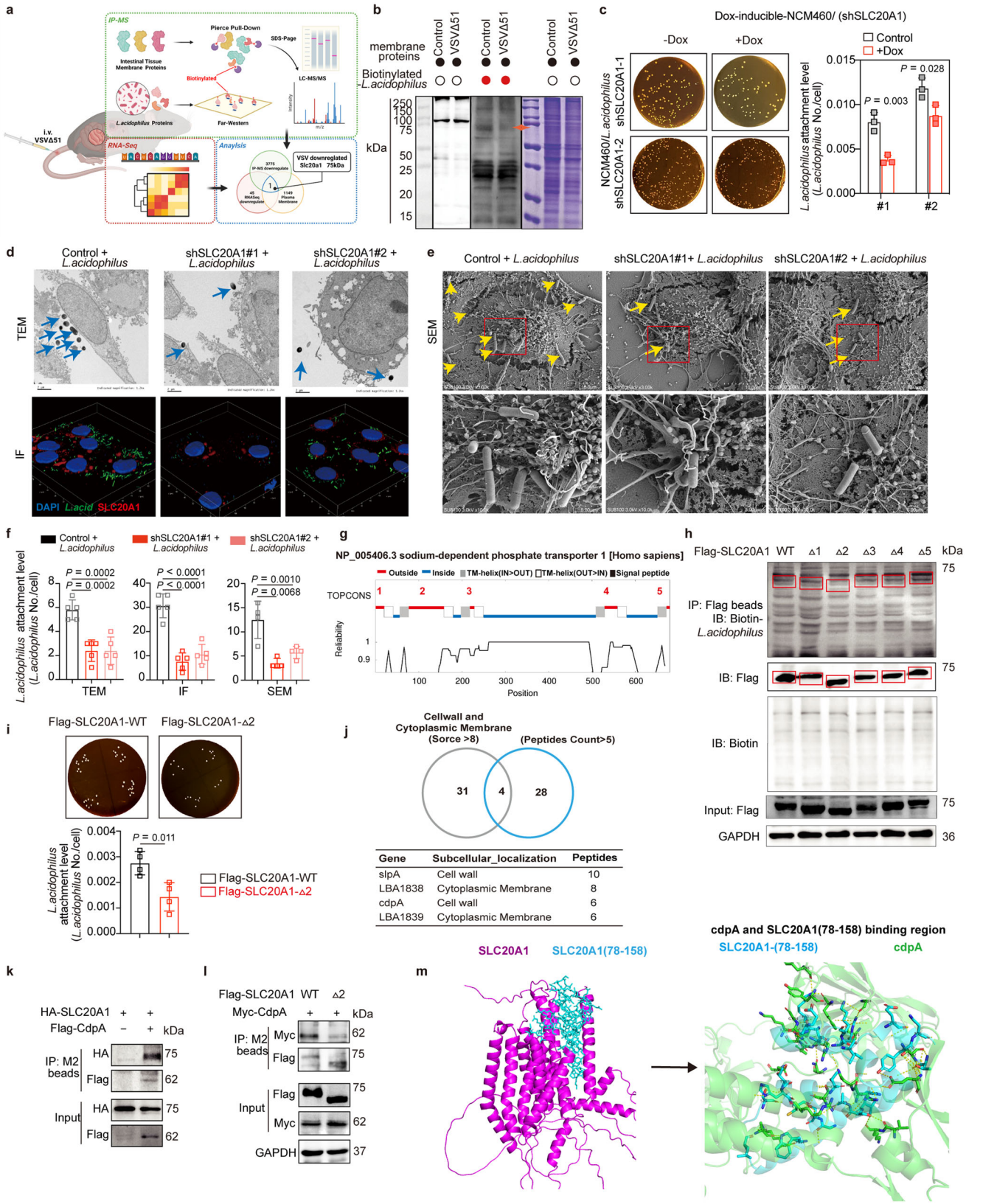

suspension from Control or VSVΔ51-treated mice for 3 days, the microbiota-recipient mice were subjected to 1×10^7 PFUs/mouse VSVΔ51 treatment. At the end of experiments, tumor areas were calculated, and tumor tissues were dissected and fixed in 4% formaldehyde.

Cell culture, viruses and transfection

HEK-293T, NCM460, Hepa1-6, HuH7, Vero and BHK-21 cells were cultured at 37 °C in Dulbecco's Modified Eagle Medium (DMEM)(10-013-CV, Corning Cellgro, USA) supplemented with 10% fetal bovine serum (FBS)(35-010-CV, Corning Cellgro, USA). H22 cells were cultured at

Fig. 7 | VSVΔ51 downregulates SLC20A1, thereby decreasing the attachment of *L. acidophilus* to intestinal tissue and subsequent gut colonization. a Schematic of the screening of *Lactobacillus* receptor. RNA-seq was performed from mice intestinal epithelial tissues with or without VSVΔ51 treatment and differentially expressed genes (DEGs) were analyzed. *L. acidophilus* proteins were collected and labeled with biotin. Streptavidin pull-down and mass spectrometry were performed. Venn diagram was performed based on DEGs, pull-down proteins and membrane proteins, which SLC20A1 was identified.Created in BioRender. Yang, X. (2025) https://BioRender.com/s68y847. **b** Biotinylation-based Far-Western detected a protein band loss in VSVΔ51 treatment group. **c**–**f** KD of SLC20A1 showing reduced attachment of *L. acidophilus* on NCM460 cells as determined by adhesion assay ($n = 3$/group), TEM ($n = 5$/group), bacteria staining with IF ($n = 5$/group) and SEM ($n = 4$/group). Quantitation data of each assay for the bacterial count were shown. Dox, doxycycline (200 ng ml^{-1}). **g** TOPCONS analysis of SLC20A1 membrane protein topology. **h** The second domain (78-158 aa) of SLC20A1 was bound to the *L. acidophilus*. NCM460 protein lysis was subjected to SDS-PAGE; Biotin-labeled *L. acidophilus* proteins were incubated and far-western was performed. **i** The attachment of *L. acidophilus* as determined by adhesion assay($n = 4$/group). **j** SLC20A1 binding proteins from *L. acidophilus* protein were determined by IP-MS. **k** Immunoprecipitation analysis of the binding between SLC20A1 and CdpA in HEK-293T cells. **l** The second domain (78–158 aa) of SLC20A1 binds to CdpA in HEK-293T cells based on Immunoprecipitation analysis. **m** Modeling the binding between the second domain of SLC20A1 and CdpA complex by SWISSMODEL.EXPASY and PyMOL. **c**, **i** Two-tailed Student's *t*-test. **f** One-way ANOVA. Results are presented as mean ± S.D. Each spot represents one subject. Source data are provided in the Source Data file. See also Supplementary Fig. 6.

37 °C in Roswell Park Memorial Institute 1640 (RPMI 1640) (10-040-CV, Corning Cellgro, USA) supplemented with 10% FBS.

The cell lines have been authenticated by the short tandem repeat (STR) assay and were confirmed to be without mycoplasma contamination. VSVΔ51-GFP was provided by Prof. Haipeng Zhang (School of Medicine, Jinan University). HSV-1-anti-PD1 was provided by Prof. Minfeng Shu (School of Basic Medical Sciences, Fudan University). VACV(WR)-GFP was purchased from VectorBuilder company. VSVΔ51 was propagated in BHK-21 cells, VACV-GFP and HSV-1 were propagated in Vero cells. Virus titer was determined by TCID50 assay using BHK-21 cells and converted to PFU.

All transient transfections of plasmids and shRNA into cell lines followed the standard protocol for Lipofectamine 3000 Transfection Reagent (L3000001, Thermo Fisher, USA). Cell viability was measured by 2-(2-methoxy-4-nitrobenzene)-3-(4-nitrobenzene)-5-(2, 4-disulfonyl benzene)-2h-tetrazole monosodium salt bromide (CCK8) (K1018, APExBIO, USA) assay after 48 h post-infection.

Bacteria and culture conditions

Clostridium aldenense (DSM 19262), *Clostridium bolteae* (ATCC BAA-613), *Clostridium lavalense* (DSM 19851), *Clostridium scindens* (CCUG 45363), *Clostridium polysaccharolyticum* (DSM 1801), *Barnesiella viscericola* (DSM 18177), *Barnesiella intestinihominis* (DSM 21032), *Blautia hansenii* (DSM 20583), *Blautia wexlerae* (DSM 19850), *Desulfovibrio oxamicus* (DSM 1925), *Desulfovibrio simplex* (DSM 4141), *Desulfovibrio piger* (DSM 749), *Rikenella microfusus* (DSM 15922), *Acetatifactor muris* (DSM 23669), and *Lactobacillus apodemi* (DSM 16748) were purchased from Ning bo testobio Co., Ltd. *Klebsiella oxytoca* (GDMCC 1.134), *Alistipes shahii* (DSM 19121 = ATCC BAA-1179 = CCUG 48947), *Alistipes onderdonkii subsp. Onderdonkii* (DSM 19147 = ATCC BAA-1178 = CCUG 48946), *Alistipes finegoldii* (DSM 17242), *Alistipes indistinctus* (DSM 22520), *Ligilactobacillus animalis* (CGMCC 1.1852), *Lacticaseibacillus paracasei* (ATCC 334), *Lactobacillus fermentum* (ATCC 11739), *Clostridium methylpentosum* (ATCC 43829), *Lactobacillus salivarius* (ATCC 11741), *Lactobacillus acidophilus* (CICC 20244) and *Akkermansia muciniphila* (ATCC BAA-835) were purchased from Guangdong Microbial Culture Collection Center (GDMCC).

Akkermansia muciniphila and *Clostridium lavalense* cultured in Brain Heart Infusion (BHI) broth (MZM0090, MINGZHOUBIO, China) at 37 °C under aerobic conditions for 48 h before use. *Desulfovibrio piger*, *Desulfovibrio oxamicus*, and *Desulfovibrio simplex* were cultured in Desulfovibrio Medium Base (MZM2256, MINGZHOUBIO, China) at 37 °C under aerobic conditions for 48 h before use. *Klebsiella oxytoca* cultured in Nutrient Agar broth (HB8274-1, Hopebio, China) at 37 °C under aerobic conditions for 48 h before use. *Rikenella microfusus* cultured in Columbia Blood Agar Base broth (CP0160, HuanKai Microbial, China) at 37 °C under aerobic conditions for 48 h before use. *Alistipes shahii*, *Alistipes finegoldii, Alistipes indistinctus* and *Alistipes onderdonkii subsp. Onderdonkii* cultured, *Clostridium aldenense, Clostridium scindens, Barnesiella viscericola*, and *Barnesiella intestinihominis* in Chopped Meat Broths (MZM5638, MINGZHOUBIO, China) at 37 °C under aerobic conditions for 48 h before use. *Clostridium bolteae* in Gifu Anaerobic Medium broth (TYSW33987, Ning bo testobio Co., Ltd, China) at 37 °C under aerobic conditions for 48 h before use. *Clostridium lavalense* and *Clostridium polysaccharolyticum, Clostridium methylpentosum* and cultured in Chopped Meat Carbohydrate Broth (CMC) (KDM150, MINGZHOUBIO, China) at 37 °C under anaerobic conditions. *Blautia hansenii, Blautia wexlerae*, and *Acetatifactor muris* were cultured in PYG MEDIUM (modified) (KDM144, MINGZHOUBIO, China) at 37 °C under anaerobic conditions. *Lacticaseibacillus paracasei, Lactobacillus apodemi, Ligilactobacillus animalis, Lactobacillus fermentum*, and *Lactobacillus salivarius, Lactobacillus acidophilus* cultured in MRS Medium (27315, HuaiKai Microbial, China) at 37 °C under anaerobic conditions, respectively. Chopped Meat Broths, Gifu Anaerobic Medium broth and Chopped Meat Carbohydrate Broth The configuration of a required an additional 20% minced meat pellet, Vitamin K1 Solution (500 mg mL^{-1}) and Heme chloride solution (50 mg mL^{-1}).

Cell-bacteria co-culture

As we reported previously, the bacteria were collected for the co-culture of epithelial cells with bacteria. HuH7 cell were seeded on 48-well plates at 1×10^5 cells per well for 24 h and treated with bacteria at different MOI (100 MOI, 200 MOI) for 2 h. After 2 h, the supernatant was aspirated. Cells were washed 5 times using sterile PBS. Fresh antibiotics (1% penicillin/streptomycin, 15140-122, GIBCO, USA) containing medium. VSVΔ51 (0.01 MOI) was used to infect cells in DMEM supplemented with 10% FBS containing serum for 2 h. Afterward, the supernatant was removed and replaced with fresh medium. Cell viability was assessed 48 h later. Cell viability was measured by CCK8 (K1018, APExBIO, USA) assay.

Antibiotics treatment

To ablate the gut microbiome and/or the tumor microbiome, 6-week-old mice were administered an antibiotic cocktail (ABX) as described[31]. Briefly, mice started to be administered with high dose of antibiotics (300 µL each mouse), containing vancomycin (50 mg mL^{-1}; V105495, Aladdin, China), imipenem/cilastatin (25 mg mL^{-1}; C304719, I304258, Aladdin, China), neomycin (10 mg mL^{-1}; N412785, Aladdin, China), and amphotericin (1 mg mL^{-1}; A105482, Aladdin, China), by oral gavage daily for 3 consecutive days. Then the mice were treated with a low-dose ABX containing vancomycin (0.5 mg mL^{-1}), imipenem/cilastatin (0.5 mg mL^{-1}), neomycin (1 mg mL^{-1}), and amphotericin (0.5 mg mL^{-1}), by the sterile drinking water until endpoints. Solutions and bottles were changed every other day due to the short half-life of imipenem. To specifically eliminate the intratumoral microbiota, we chose an intravenous injection of 300 µL of the ABX suspension daily (vancomycin 10 mg mL^{-1}; imipenem/cilastatin 4 mg mL^{-1}; Neomycin 1.5 mg mL^{-1}).

Feces 16S rRNA sequencing and data analysis

DNA extraction and PCR amplification. Briefly, DNA extraction was performed using BGI-NGS-TQ-DNA method (Meta DNA protocol). DNA

library preparation and 16S rRNA gene sequencing were performed by The Beijing Genomics Institute (BGI, China) and CHI BIOTECH CO., LTD. The V3-V4 regions of 16S rRNA genes were amplified using specific primer (341F-'CCTAYGGGRBGCASCAG'and 806R-'GGACTACNNGGGTATCTAAT') together with the barcode.

Illumina sequencing. Purified amplicons were pooled in equimolar amounts and paired-end sequenced on an MGISEQ-2000 platform (BGI, Beijing, China) according to the standard protocols by BGI.

Amplicon sequence processing and contamination DNA filtration. The 16S rRNA sequencing data were quality-filtered and analyzed using QIIME2 (version 2019.4.0; default parameters) software. The sequencing errors and replicated sequences were determined by Deblur algorithm with default parameters. Raw data are filtered, and high-quality clean reads are generated. After chimera sequences filtering, the dereplicated sequences were classified taxonomically through Ribosomal Database Project (RDP) 16S rRNA gene reference database at a 99% identity cut-off by USEARCH (v7.0.1090) software. OTU representative sequences are aligned by RDP classifier (v2.2) software (sequence identity is set to 0.6).

Data analysis. Alpha diversity indices including Chao1, Shannon index, principal coordinate analysis (PCoA) based on Bray-curtis dissimilarity and the PERMANOVA test were all calculated by Vegan v2.6-4 package. Proportional Chord Diagram analysis was all calculated by "circlize" package. The linear discriminant analysis (LDA) effect size (LEfSe) (http://huttenhower.sph.harvard.edu/LEfSe) was all calculated by "microeco" package (LDA score > 2, $P < 0.05$). Stacked bar plot analysis was all calculated by "MicrobiotaProcess" package. Mantel test analysis was calculated by "linkET" package.

Tissues 5 R (5 regions) 16S rRNA sequencing and data analysis

DNA extraction and PCR amplification. Liver tumor samples were collected, and total microbial genomic DNA was extracted using the FastPure Stool DNA Isolation Kit (Magnetic bead) (MJYH, shanghai, China) according to manufacturer's instructions. The quality and concentration of DNA were determined by 1.0% agarose gel electrophoresis and a NanoDrop® ND-2000 spectrophotometer (Thermo Scientific, USA).

16S rRNA amplification and sequencings were done by amplifying 5 regions on the 16S rRNA gene in multiplex by T100 Thermal Cycler (BIO-RAD, USA). The negative controls contain sampling negative controls, DNA extraction controls and no-template PCR amplification controls.

Illumina sequencing. Purified amplicons were pooled in equimolar amounts and paired-end sequenced on an Illumina NextSeq 2000 platform (Illumina, San Diego, USA) according to the standard protocols by Majorbio Bio-Pharm Technology Co. Ltd. (Shanghai, China).

Amplicon sequence processing and contamination DNA Filtration. Reads were demultiplexed per sample, filtered and aligned to each of the five amplified regions based on the primers' sequences. To combine read counts from the five regions into a coherent profiling result, the Short MUltiple Regions Framework (SMURF) method was applied. The GreenGenes database (May 2013 version, with some improvements) was used as reference[29,63]. To reduce the noise variation, samples with <1000 normalized reads (including negative controls) and species with relative abundances of <10−4 were discounted from further analysis. Any species that was prevalent across >7.5% of negative DNA/PCR/Sequencing controls or >7.5% of empty paraffin controls was completely removed[64].

Data analysis. Same as Feces 16S rRNA sequencing data analysis.

Measurement of viral mRNA levels and titers

VSVΔ51-infected mice were euthanized 3 days post infection. Organs or tissues such as heart, liver, spleen, lung, kidney, brain, anker and tumor were harvested, weighed, and homogenized. The remaining cells were resuspended in TRIzol (15596018, ThermoFisher, USA), and RNA was extracted according to the manufacturer's recommendation. VSVΔ51 RNA levels were determined by one-step quantitative reverse transcriptase PCR (qRT−PCR) using an RT-PCR kit (A1250, PROMEGA, USA) on a Roche Instrument using standard cycling conditions. For some samples, the viral titers were determined by $TCID_{50}$ assay on BHK-21 cells as described[65].

Phylogenetic analysis for bacteria

The 16S rRNA sequences of Bacteria were downloaded from NCBI and used as a reference genome. To construct a phylogenetic tree through identified strains, the Basic Local Alignment Search Tool (BLAST) was used to analyze the obtained sequence with organisms in the GeneBank database. The Neighbor Joining algorithm in MEGAX software was used to construct the phylogenetic tree and molecular evolutionary analyses. The percentage of replicate trees where the associated taxa clustered together in the bootstrap test (1000 replicates) was shown next to the branches. The Maximum Composite Likelihood method was used to compute the evolutionary distances[66]. The bacterial 16S rRNA sequences used are listed in Supplementary Data 2.

Flow cytometry

Tumors samples were harvested after perfusion with PBS. Tumor samples were obtained, subjected to single cell suspension and passed through a 70 mm filter. Erythrocytes were lysed through Red Blood Cell Lysis Buffer (R874904, MACKLIN, USA), and the remaining cells were resuspended in PBS supplemented with 2% fetal bovine serum (35-010-CV, Corning, USA) and 1 mM EDTA (E762089, MACKLIN, USA) and maintained on ice. Fluorochrome-conjugated anti-mouse antibodies from BioLgend were used. Utilizing cell stimulation cocktail (1:500, 00-4975-93, ThermoFisher, USA) induction followed by intracellular detection of cytokines and secreted proteins in ex vivo cells. Dead cells were stained with Zombie Red™ Fixable Viability kit (423110, BioLegend, USA). The staining for cell surface antigens was performed. Cells were fixed using True-Nuclear™ Transcription Factor Buffer Set (424401, BioLegend, USA) and Cyto-Fast™ Fix/Perm Buffer Set (BioLegend, 426803, USA) processed for flow cytometry assay (Beckman Coulter). Data were acquired with CytoFLEX and analyzed using FlowJo. The gate strategy was set based on isotype control. Technicians acquiring and gating the data were blinded to the treatments. Schematic gating strategy is provided in Supplementary Fig. 8.

Western blot

Cells or tissues were lysed using NP-40 buffer[36]. The protein in SDS-PAGE (10%-12%) was then transferred onto polyvinylidene difluoride (0.45 μm, PVDF) membranes (ZY101123, Millipore, USA) for about 260 V 2.5 h, which was then blocked with 5% non-fat milk in 0.05% Tris-based saline-Tween 20 for 1 h at room temperature. The membranes were incubated with primary antibodies overnight at 4 °C and then with secondary antibody at room temperature for 1 hr. The antibodies used in this study are shown in the essential resources Supplementary Data 1. For immunoprecipitation, cell lysates were incubated with indicated antibodies for 3 h at 4 °C.

Antibodies and reagents

Antibodies used in this study are listed as follows: GAPDH (60004-1-Ig, Proteintech, 1:10000), HA Tag (51064-2-AP, Proteintech, 1:4000), Myc-Tag (9B11) (2276 s, Cell Signaling Technology, 1:2000), FLAG M2 Sigma F1804 1:2000), Cleaved Caspase-3 (Asp175) (5A1E) (9664 P,Cell Signaling Technology, 1:200 (IHC)), Ki67 (34330, Cell Signaling Technology, 1:800 (IHC)), SLC20A1 (12423-1-AP, Proteintech, 1:1000 (WB)

1:200 (IF)), Occludin (502601, ZEN-BIOSCIENCE, 1:1000), E-Cadherin (3195 s, Cell Signaling Technology, 1:1000), Stat3 (D3ZZ2G) (12640, Cell Signaling Technology, 1:1000), Phospho-Stat3 (Tyr705) (D3A7) (9145, Cell Signaling Technology, 1:1000), VSV-G[8G5F11] (EB0010, Kerafast,1:1000 (WB) 1:100 (IHC)), Stat1 (D1K9Y) (14994, Cell Signaling Technology, 1:1000), Phospho-Stat1 (Tyr701) (58D6) (9167, Cell Signaling Technology, 1:1000), Goat anti-Rabbit IgG (H + L) Secondary Antibody HRP (31460, Thermo Fisher, 1:10000), Goat anti-Mouse IgG (H + L) Secondary Antibody HRP (31430, Thermo Fisher, 1:10000), Ultra Streptavidin-HRP (RG235220, Thermo Fisher Scientific, 1:10,000), CD45.2 APC/Fire 750 (109852, BioLegend, USA, 1:200), CD3 FITC (100204, BioLegend, 1:200), CD4 Brilliant Violet 421 (100438, BioLegend, 1:200), CD8a Brilliant Violet 510 (100752, BioLegend, 1:200), IFN-γ Brilliant Violet 605 (505804, BioLegend, 1:200), TNF-α APC (506308, BioLegend, 1:200), Granzyme B PE (372208, BioLegend, 1:200), FOXP3 PF (126404, BioLegend, 1:200), CD25 PE/Cyanine7 (102016, BioLegend, 1:200), CD11b APC (101211, BioLegend, 1:200) and F4/80 PE/Cyanine7 (123114, BioLegend, 1:200)

Immunoprecipitation and pull-down assays

For FLAG/Myc-tagged protein immunoprecipitation, transfected cells were collected and lysed in NP-40 buffer supplemented with protease and phosphatase inhibitor cocktail (B15002, Bimake, USA). Cell lysates were incubated with indicated antibodies (M2, A222, Sigma-Aldrich /Myc beads, B26302, Biotool, USA) for 3 h at 4 °C. The beads were washed and boiled with 50 µL loading buffer and were subjected to SDS-PAGE.

Reverse transcription-quantitative PCR (RT-qPCR)

Total RNA was extracted using TRIzol (15596018, ThermoFisher, USA), and reverse transcription was performed from 2 µg total RNA and reverse transcribed using RevertAid Reverse Transcriptase (22948, PROMEGA, USA) according to the manufacturer's recommendation. qRT-PCR was performed with SuperReal PreMix SYBR Green (A4004S, BIMAKE, USA) using a Roche480 Real-Time PCR Detection System (Roche480, Roche, USA). All genes were normalized to *β-ACTIN/β-Actin*. The primer sequences used are listed in Supplementary Table 1.

RNA sequencing and data processing

Total RNA was extracted from the cells using Trizol (ThermoFisher) according to the manual and sent to Pangu Medical Technology Co., Ltd (Guangdong, China) for further processing and RNA-seq analysis. In brief, total RNA was qualified and quantified using a NanoDrop and Agilent 2100 bioanalyzer (Thermo Fisher Scientific, USA), and qualified library sequenced using illumina Novaseq 6000. The raw reads with adapters and low-quality bases were filtered by fastp[67]. Fragments Per Kilobase of transcript per Million mapped reads (FPKM) of each gene was calculated based on the length of the gene and the number of reads mapped to this gene.

Differential gene expression and enrichment analysis

Differential gene expression between the two groups of different treatments were analyzed using the DESeq2 R package[68]. The *P-values* were adjusted using the Benjamini&Hochberg method. A corrected *P*-value < 0.05 (FDR = 5%) and absolute fold change ≥ 2 was set as the threshold for significantly different expression genes (DEGs). Cluster Profiler tool was used to perform gene enrichment analysis. GSEA enrichment scores were calculated using the R package GSVA[69].

Lentivirus production and infection

All of the plasmids were purchased from Addgene. We screened ~4 hairpin shRNAs targeting specific transcript and found at least two independent sequences that reduced mRNA levels by >70%. These shRNAs were in the pLKO.1 vector. Lentiviruses were produced in HEK-293T cells using 10 µg shRNA plasmid, 5 µg psPAX2 plasmid and 5 µg pMD2.G. The supernatants containing viral particles were harvested at 48 and 72 h after transfection and were filtered through Millex-GP Filter Unit (0.45 µm pore size, Millipore). Cells were introduced with lentivirus, 200 µL FBS, 5 µg mL^{-1} polybrene (TR-1003-G, Millipore, USA) for 48 h. Cells were selected with 2 µg mL^{-1} puromycin for 3–4 days to increase the KD efficiency. After selection, 200 ng mL^{-1} doxycycline (Dox) was added to induce KD of the target gene.

DNA construction and mutagenesis

PCR-amplified *SLC20A1*, *Cdpa*, *LBA1838*, *SlpA*, *LBA1838* and *LBA1839* were cloned into pcDNA3.1. All the mutations were generated by Mut Express II Fast Mutagenesis Kit (C214-01/02, Vazyme, China) according to the manufacturer's instructions. All constructions with the desired insertions or mutations were confirmed by sequencing.

Immunofluorescence (IF) and Fluorescence in Situ Hybridization (FISH) assay

Immunofluorescence staining was performed on paraffin-embedded tissue sections. Tissue sections were incubated with primary antibodies at a dilution of 1:100, fluorescence dye-conjugated secondary antibodies and DAPI according to standard protocols. Cy5.5-labeled *L. acidophilus* probe (sequence: 5'-TCTTTCGATGCATCCACA-3') was used to detect *L. acidophilus* colonization in paraffin-embedded intestine sections. FITC-labeled 16S EUB338 probe (sequence: 5'-GCTGCCTCCCGTAGGAGT-3') was used to detect *bacteria* colonization in paraffin-embedded intestine sections. FITC-labeled Live/Dead Bacterial Double Stain Kit (share-bio, SB-L6060L, USA) was used to detect bacteria adhesion in NCM460. Images were acquired with a confocal microscope (Leica).

Transmission electron microscopy (TEM)

NCM460 cells with or without SLC20A1 KD were seeded in sterile coverslips and co-cultured with *L. acidophilus* (MOI = 100) for 2 h. Cell samples were collected with centrifugation. Colonic tissues were dissected into small pieces. All the samples were fixed in 2.0% glutaraldehyde in 0.1 M sodium cacodylate (G1102-100ML, Electron Microscopy Sciences, Servicebio, China). Samples were then submitted to the Electron Microscopy Facility (Servicebio) for standard transmission electron microscopy ultrastructural analysis.

Scanning electron microscopy (SEM)

NCM460 cells with or without SLC20A1 KD were seeded in sterile coverslips and co-cultured with *L. acidophilus* (MOI = 100) for 2 h. Cells were then washed with freshly prepared Sorensen' phosphate buffer (0.1 M, pH 7.2) three times and were fixed with 2.5% glutaraldehyde fixative overnight. After dehydration and coating with gold-palladium, specimens were examined by a Cold Field Scanning Electron Microscope (Hitachi SU8100, Guang Tenng Technology CO.,LTD).

Chromatin immunoprecipitation assay (ChIP)

NCM460 cells pre-treated with or without IL-6 were crosslinked with 1% formaldehyde for 10 min at room temperature and quenched by glycine. After cell lysis, the chromatin was fragmented into 100–500 bp by Bioruptor Sonicator (Diagenode) and protein-DNA complexes were immunoprecipitated (IP) by 5 mg mouse monoclonal antibody against human Phospho-STAT3 (Tyr705) (9145, CST, USA), RNA Polymerase II, clone CTD448 or anti-IgG antibody (17-371, Millipore, USA). Dynal magnetic bead was added and mixed on rotator at 4 °C overnight. Contaminating RNA was removed by treating with 10 µg mL^{-1} RNase A. After washing and reversal of crosslinks, the IP and input DNA was amplified by real-time PCR with primers near the putative *IL-6*-binding site in the *SLC20A1* promoter.

Cytokines array
Mice sera were collected and send to the Shanghai Universal Biotech Co., Ltd company for detection of 23 cytokine group I factors using the Bio-Plex 200 assay kit.

Hematoxylin-eosin staining (H&E) and Immunohistochemistry (IHC) assay
Tissue pathological observations, cell death and proliferation markers were measured by H&E staining and IHC staining, respectively. The expression of Ki-67, cleaved-Caspase-3 (34330, 9664 P, Cell Signaling Technology, USA) and VSV-G (EB0010, Kerafast, USA) in tumors was assessed by IHC. Briefly, for H&E staining, tissues were immobilized with 10% neutral-buffered formalin and embedded in paraffin. The sections (5 mm) were deparaffinized with xylene and rehydrated through washing with graded ethanol. For IHC staining, the sections were dewaxed in xylene, hydrated in descending concentrations of ethanol, immersed in 0.3% H_2O_2-methanol for 30 min. The sections were further washed with phosphate-buffered saline and probed with indicated antibodies or isotype control at 4 °C overnight. After washing, biotinylated goat anti-rabbit or anti-mouse IgG were incubated at room temperature for 2 h. Immunostaining was visualized with streptavidin/peroxidase complex and diaminobenzidine, and sections were then counterstained with hematoxylin. All slides were observed and captured under a microscope (SQS-1000, TEKQSRAY, China) and at least three fields for each slide were randomly selected for qualification by ImageJ software.

L. acidophilus attachment assay
NCM460 cells were co-cultured with *L. acidophilus* (MOI = 200) for 2 h under aerobic conditions. After co-culture, the cells were washed 5 times with PBS and subsequently lysed for 5 min with 500 µL ice-cold PBS with Tween 80 (0.01%). The samples were then diluted 10-, 100-, and 1000-fold and plated onto a BHI agar plate. After overnight incubation at 37 °C, the number of colony formation units (CFU) was counted.

L. acidophilus surface proteins extraction
To prepare the *L. acidophilus* surface proteins, *L. acidophilus* was first cultured at 37 °C under aerobic conditions for 24 h. The bacteria cells were then collected by centrifugation at 2000 g for 15 min at 4 °C. The bacteria pallets were washed 3 times by PBS and the wet pallet was weighted. Approximately 3 mL lysis buffer (50 mM Tris-HCl, pH 8.0, 1 mM EDTA, 50 mM NaCl, 1 mM phenylmethylsulfonylfluoride) with lysozyme (300 µg mL^{-1}) for each wet gram of *L. acidophilus* pallet was added to resuspend the pallet. The whole suspension was stirred for 30 min at 4 °C, which was then treated with 1% triton x-100 (v/v) and applied for ultrasound sonication. The sonicated *L. acidophilus* suspension was further incubated at room temperature with DNase1 (10 mg kg^{-1}) and $MgCl_2$ (10 mM) for 15 min to remove the viscous nucleic acid. The suspension was centrifuged at 10,000 g for 15 min at 4 °C to remove the pallets, and the supernatant was collected and used as the surface membrane proteins for further identification of the protein of interest.

Biotin pull-down assay and protein identification
The extracted biotinylated *L. acidophilus* protein and NCM460 lysates were incubated with streptavidin magnetic beads (88816, Thermo Fisher Scientific, USA) for 4 h at 4 °C. The streptavidin bound *L. acidophilus* proteins were incubated with NCM460 proteins overnight at 4 °C, and subsequently washed with lysis buffer 5 times. The NCM460-*L. acidophilus* interacting proteins were eluted by heating in 50 µL of 2 × loading buffer at 100 °C. Eluted proteins were subjected to SDS-PAGE and the whole gel was then subjected to Coomassie brilliant blue G250 method staining (P0017, Beyotime, China) following the manufacturer's instructions. The extraction, detection, and quantitative analysis of protein profiling in the samples were performed by Wuhan Metware Biotechnology Co., Ltd. (www.metware.cn). LC was performed on a nanoElute UHPLC (Bruker Daltonics, Germany). About 200 ng peptides were separated within 40 min at a flow rate of 0.3 µL min^{-1} on a commercially available reverse-phase C18 column with an integrated CaptiveSpray Emitter (25 cm × 75 µm ID, 1.6 µm, Aurora Series with CSI, IonOpticks, Australia). The LC was coupled online to a hybrid timsTOF Pro2 (Bruker Daltonics, Germany) via a CaptiveSpray nano-electrospray ion source (CSI). The capillary voltage for mass spectra and mass spectrum acquisition was set to 1500 *V* and ranged from 100 to 1700 *m/z*. MS raw data were analyzed using DIA-NN(v1.8.1) with library-free method the uniprot-proteome_UP000000589_M database(A total of 55319 sequences) was uesed to creat a spectra library with deep learning algrithms of neural networks.The MBR method was used to create a spectral library from the DIA data, which was then used for reanalysis. FDR of search results was adjusted to <1% at both protein and precursor ion levels, the remaining identifications were used for further quantification analysis. Mass spectrometry results show in Supplementary Data 3 and 4.

Far western assay and protein identification
For the screening of the NCM460 surface receptor that binds to *L. acidophilus*, the NCM460 proteins were separated by SDS-PAGE and transferred onto a PVDF membrane. The PVDF membrane was blocked with 5% BSA for 1 hr and incubated with biotinylated *L. acidophilus* surface proteins (final concentration 0.05 µg $µl^{-1}$) overnight at 4 °C, Biotin-labeled proteins were detected using Ultra Streptavidin-HRP (RG235220, Thermo Fisher Scientific, USA) (1:10000).

Targeted metabolomics assay
To extract metabolites from the samples, 800 µL of cold Methanol/Acetonitrile/Water (2:2:1, *v/v*) extraction solvent was added to 100 mg sample, and adequately vortexed. For absolute quantification of the metabolites, stock solutions of stable-isotope internal standards were added to the extraction solvent simultaneously. Then the samples were under vigorous shaking for 2 min at 4 °C incubated on ice for 20 min, and then centrifuged at 14,000 g for 20 min at 4 °C, the supernatant was collected and flowed through a 96-well protein precipitation plate, and then the elution was collected and dried in a vacuum centrifuge at 4 °C. For LC-MS analysis, the samples were re-dissolved in 100 µL Acetonitrile/Water (1:1, *v/v*) solvent and centrifuged at 14000 g at 4°C for 15 min, then the supernatant was injected. LC-MS/MS analyses were performed using an UHPLC (1290 Infinity LC, Agilent Technologies) coupled to a QTRAP MS (6500 + , Sciex) in Shanghai Applied Protein Technology Co., Ltd. HILIC separation was then initiated at a flow rate of 300 µL min^{-1}. RPLC separation was then initiated at a flow rate of 400 µL min^{-1}. MultiQuant or Analyst was used for quantitative data processing. After and normalization, the data were uploaded to SIMCA-P (v14.1, Umetrics, Umea, Sweden) for multivariate data analysis: orthogonal partial least squares discriminant analysis (OPLS-DA). The stability of the model was evaluated using 7-fold cross validation and response permutation test. The importance (VIP) value of each variable in the OPLS-DA model was calculated to indicate its contribution to classification. Significance was determined by unpaired *t*-tests. $P < 0.05$ was considered statistically significant.

Statistics and reproducibility
Statistical significance was performed using GraphPad Prism version 9.0 (La Jolla, CA). The specific test for each dataset is indicated in respective figure legends and was selected by the number of comparison groups and variance of the data. Significance was determined by unpaired one- or two-tailed Student's *t*-test, Fisher's Exact test, Mann–Whitney *U*-test, or ANOVA with Tukey post-hoc test. one-tailed Fisher's Exact test was used for enrichment analysis of GO terms and

KEGG pathways. The number of independent biological replicates are provided in the figures and figure legends. No statistical method was used to predetermine sample size. No data were excluded from the analyses. The experiments were not randomized, and the investigators were not blinded to allocation during experiments and outcome assessment.

Reporting summary

Further information on research design is available in the Nature Portfolio Reporting Summary linked to this article.

Data availability

All data presented in the manuscript and Supplementary Figures are provided in the Excel file as the Source Data file, which is linked to this manuscript. The raw sequence data reported in this study are available in the Genome Sequence Archive (Genomics, Proteomics & Bioinformatics 2021) in National Genomics Data Centre (Nucleic Acids Res 2022), China National Centre for Bioinformation/Beijing Institute of Genomics, Chinese Academy of Sciences database under the Bioproject number PRJCA027376 (GSA: CRA017533, CRA022843, CRA017504, CRA0175502 and CRA017489) that are publicly accessible at https://ngdc.cncb.ac.cn/gsa. The protein mass spectrometry data generated in this study have been deposited in the ProteomeXchange database under accession code PXD061574 and PXD061642 [http://www.proteomexchange.org]. The authors declare that the remaining data generated or analyzed during this study are available within the article, Supplementary Information, or Source Data file. Source data are provided with this paper.

References

1. Lafaro, K. J., Demirjian, A. N. & Pawlik, T. M. Epidemiology of hepatocellular carcinoma. *Surg. Oncol. Clin. N. Am.* **24**, 1 (2015).
2. Global Burden of Disease Cancer C. et al. The global burden of cancer 2013. *JAMA Oncol.***1**, 505–527 (2015).
3. Rimassa, L., Finn, R. S. & Sangro, B. Combination immunotherapy for hepatocellular carcinoma. *J. Hepatol.* **79**, 506–515 (2023).
4. Shalhout, S. Z., Miller, D. M., Emerick, K. S. & Kaufman, H. L. Therapy with oncolytic viruses: progress and challenges. *Nat. Rev. Clin. Oncol.* **20**, 160–177 (2023).
5. Yoo, S. Y., Badrinath, N., Woo, H. Y. & Heo, J. Oncolytic virus-based immunotherapies for hepatocellular carcinoma. *Med. Inflamm.* **2017**, 5198798 (2017).
6. Zhang, H. et al. Targeting VCP enhances anticancer activity of oncolytic virus M1 in hepatocellular carcinoma. *Sci. Trans. Med.* **9**, eaam7996 (2017).
7. Samson, A. et al. Oncolytic reovirus as a combined antiviral and anti-tumour agent for the treatment of liver cancer. *Gut.* **67**, 562–573 (2016).
8. Zhu, L. et al. Recent advances in oncolytic virus therapy for hepatocellular carcinoma. *Front. Oncol.* **13**, 1172292 (2023).
9. Heo, J. et al. Randomized dose-finding clinical trial of oncolytic immunotherapeutic vaccinia JX-594 in liver cancer. *Nat. Med.* **19**, 329–336 (2013).
10. Webb, M. J. et al. Expression of tumor antigens within an oncolytic virus enhances the anti-tumor T cell response. *Nat. Commun.***15**, 5442 (2024).
11. Altomonte, J. et al. Antifibrotic properties of transarterial oncolytic VSV therapy for hepatocellular carcinoma in rats with thioacetamide-induced liver fibrosis. *Mol. Ther.* **21**, 2032–2042 (2013).
12. Shinozaki, K., Ebert, O. & Woo, S. L. Eradication of advanced hepatocellular carcinoma in rats via repeated hepatic arterial infusions of recombinant VSV. *Hepatology* **41**, 196–203 (2005).
13. Ebert, O., Shinozaki, K., Huang, T. G., Savontaus, M. J., Garcia-Sastre, A. & Woo, S. L. Oncolytic vesicular stomatitis virus for treatment of orthotopic hepatocellular carcinoma in immune-competent rats. *Cancer Res.* **63**, 3605–3611 (2003).
14. Chen, X. et al. IDH1 mutation impairs antiviral response and potentiates oncolytic virotherapy in glioma. *Nat. Commun.* **14**, 6781 (2023).
15. Xiao, J. et al. CDK4/6 inhibition enhances oncolytic virus efficacy by potentiating tumor-selective cell killing and T-cell activation in refractory glioblastoma. *Cancer Res.***82**, 3359–3374 (2022).
16. Tian, L. et al. Specific targeting of glioblastoma with an oncolytic virus expressing a cetuximab-CCL5 fusion protein via innate and adaptive immunity. *Nat. Cancer* **3**, 1318–1335 (2022).
17. Dai, W. et al. Overcoming therapeutic resistance in oncolytic herpes virotherapy by targeting IGF2BP3-induced NETosis in malignant glioma. *Nat. Commun* **15**, 131 (2024).
18. Xu, B. et al. An oncolytic herpesvirus expressing E-cadherin improves survival in mouse models of glioblastoma. *Nat. Biotechnol.* **37**, 102 (2018).
19. He, Y. et al. Gut microbial metabolites facilitate anticancer therapy efficacy by modulating cytotoxic CD8(+) T cell immunity. *Cell Metab.* **33**, 988–1000.e1007 (2021).
20. Brestoff, J. R. & Artis, D. Commensal bacteria at the interface of host metabolism and the immune system. *Nat. Immunol.* **14**, 676–684 (2013).
21. Baruch, E. N., Wang, J. & Wargo, J. A. Gut microbiota and antitumor immunity: potential mechanisms for clinical effect. *Cancer Immunol. Res.* **9**, 365–370 (2021).
22. Gopalakrishnan, V. et al. Gut microbiome modulates response to anti-PD-1 immunotherapy in melanoma patients. *Science* **359**, 97–103 (2018).
23. Matson, V. et al. The commensal microbiome is associated with anti-PD-1 efficacy in metastatic melanoma patients. *Science* **359**, 104–108 (2018).
24. Routy, B. et al. Gut microbiome influences efficacy of PD-1-based immunotherapy against epithelial tumors. *Science* **359**, 91–97 (2018).
25. Lee, M. H. Harness the functions of gut microbiome in tumorigenesis for cancer treatment. *Cancer Commun. (Lond)* **41**, 937–967 (2021).
26. Jia, D. et al. Microbial metabolite enhances immunotherapy efficacy by modulating T cell stemness in pan-cancer. *Cell* **187**, 1651–1665 e1621 (2024).
27. Lee, W. S. et al. Oral reovirus reshapes the gut microbiome and enhances antitumor immunity in colon cancer. *Nat. Commun.* **15**, 9092 (2024).
28. Dan, J. et al. Oncolytic virus M1 functions as a bifunctional checkpoint inhibitor to enhance the antitumor activity of DC vaccine. *Cell Rep. Med.* **4**, 101229 (2023).
29. Nejman, D. et al. The human tumor microbiome is composed of tumor type-specific intracellular bacteria. *Science* **368**, 973–980 (2020).
30. Lam, K. C. et al. Microbiota triggers STING-type I IFN-dependent monocyte reprogramming of the tumor microenvironment. *Cell* **184**, 5338–5356.e5321 (2021).
31. Fu, A. et al. Tumor-resident intracellular microbiota promotes metastatic colonization in breast cancer. *Cell* **185**, 1356–1372.e1326 (2022).
32. Dizman, N. et al. Nivolumab plus ipilimumab with or without live bacterial supplementation in metastatic renal cell carcinoma: a randomized phase 1 trial. *Nat. Med.* **28**, 704 (2022).
33. Bennett, A. & Eley, K. G. Intestinal pH and propulsion: an explanation of diarrhoea in lactase deficiency and laxation by lactulose. *J. Pharm Pharmacol.* **28**, 192–195 (1976).
34. Gao, H. et al. The functional roles of lactobacillus acidophilus in different physiological and pathological processes. *J. Microbiol. Biotechnol.* **32**, 1226–1233 (2022).

35. Ashrafian, F. et al. Comparative effects of alive and pasteurized Akkermansia muciniphila on normal diet-fed mice. *Sci. Rep.* **11**, 17898 (2021).
36. Li, K. et al. ILF3 is a substrate of SPOP for regulating serine biosynthesis in colorectal cancer. *Cell Res.* **30**, 163–178 (2019).
37. Chen, X. & Calvisi, D. F. Hydrodynamic transfection for generation of novel mouse models for liver cancer research. *Am. J. Pathol.* **184**, 912–923 (2014).
38. Long, X. et al. Peptostreptococcus anaerobius promotes colorectal carcinogenesis and modulates tumour immunity. *Nat. Microbiol.* **4**, 2319–2330 (2019).
39. Li, Q. et al. Carnobacterium maltaromaticum boosts intestinal vitamin D production to suppress colorectal cancer in female mice. *Cancer Cell* **41**, 1450–1465.e1458 (2023).
40. Tsirigos, K. D., Peters, C., Shu, N., Kall, L. & Elofsson, A. The TOPCONS web server for consensus prediction of membrane protein topology and signal peptides. *Nucleic Acids Res.* **43**, W401–W407 (2015).
41. Schiffrin, B., Radford, S. E., Brockwell, D. J. & Calabrese, A. N. PyXlinkViewer: A flexible tool for visualization of protein chemical crosslinking data within the PyMOL molecular graphics system. *Protein Sci.* **29**, 1851–1857 (2020).
42. Arulanandam, R. et al. Microtubule disruption synergizes with oncolytic virotherapy by inhibiting interferon translation and potentiating bystander killing. *Nat. Commun.* **6**, 6410 (2015).
43. Cai, J. et al. Selective replication of oncolytic virus M1 results in a bystander killing effect that is potentiated by Smac mimetics. *Proc. Natl Acad. Sci. USA* **114**, 6812–6817 (2017).
44. Shirakawa, K. et al. IL (Interleukin)-10-STAT3-galectin-3 axis is essential for osteopontin-producing reparative macrophage polarization after myocardial infarction. *Circulation* **138**, 2021–2035 (2018).
45. Liu, L. et al. Cancer-associated adipocyte-derived G-CSF promotes breast cancer malignancy via Stat3 signaling. *J. Mol. Cell Biol.* **12**, 723–737 (2020).
46. Johnson, D. E., O'Keefe, R. A. & Grandis, J. R. Targeting the IL-6/JAK/STAT3 signalling axis in cancer. *Nat. Rev. Clin. Oncol.* **15**, 234–248 (2018).
47. Castro-Mondragon, J. A. et al. JASPAR 2022: the 9th release of the open-access database of transcription factor binding profiles. *Nucleic Acids Res.* **50**, D165–D173 (2022).
48. Meisel, M. et al. Microbial signals drive pre-leukaemic myeloproliferation in a Tet2-deficient host. *Nature* **557**, 580–584 (2018).
49. Jin, C. et al. Commensal microbiota promote lung cancer development via gammadelta T cells. *Cell* **176**, 998–1013.e1016 (2019).
50. Wang, X. et al. Gut-liver translocation of pathogen Klebsiella pneumoniae promotes hepatocellular carcinoma in mice. *Nat. Microbiol.* **10**, 169–184 (2025).
51. Wei, W. et al. Parabacteroides distasonis uses dietary inulin to suppress NASH via its metabolite pentadecanoic acid. *Nat. Microbiol.* **8**, 1534–1548 (2023).
52. Anjum, N., Maqsood, S., Masud, T., Ahmad, A., Sohail, A. & Momin, A. Lactobacillus acidophilus: characterization of the species and application in food production. *Crit. Rev. Food Sci. Nutr.* **54**, 1241–1251 (2014).
53. Vemuri, R., Martoni, C. J., Kavanagh, K. & Eri, R. Lactobacillus acidophilus DDS-1 modulates the gut microbial co-occurrence networks in aging mice. *Nutrients* **14**, 977 (2022).
54. Serek, P. & Oleksy-Wawrzyniak, M. The effect of bacterial infections, probiotics and zonulin on intestinal barrier integrity. *Int. J. Mol. Sci.* **22**, 11359 (2021).
55. Salaun, C., Leroy, C., Rousseau, A., Boitez, V., Beck, L. & Friedlander, G. Identification of a novel transport-independent function of PiT1/SLC20A1 in the regulation of TNF-induced apoptosis. *J. Biol. Chem.* **285**, 34408–34418 (2010).
56. Kjellin, J. et al. Colicins and T6SS-based competition systems enhance enterotoxigenic E. coli (ETEC) competitiveness. *Gut. Microbes* **16**, 2295891 (2024).
57. Plum, M. T. W., Cheung, H. C., Iscar, P. R., Chen, Y., Gan, Y. H. & Basler, M. Burkholderia thailandensis uses a type VI secretion system to lyse protrusions without triggering host cell responses. *Cell Host Microbe.* **32**, 676–692.e675 (2024).
58. Leoni Swart, A. et al. Pseudomonas aeruginosa breaches respiratory epithelia through goblet cell invasion in a microtissue model. *Nat. Microbiol.* **9**, 1725–1737 (2024).
59. Caballero-Flores, G., Pickard, J. M. & Nunez, G. Microbiota-mediated colonization resistance: mechanisms and regulation. *Nat. Rev. Microbiol.* **21**, 347–360 (2023).
60. Lee, H. S., Gu, F., Ching, S. M., Lam, Y. & Chua, K. L. CdpA is a Burkholderia pseudomallei cyclic di-GMP phosphodiesterase involved in autoaggregation, flagellum synthesis, motility, biofilm formation, cell invasion, and cytotoxicity. *Infect. Immun.* **78**, 1832–1840 (2010).
61. Zhang, C. et al. A key genetic factor governing arabinan utilization in the gut microbiome alleviates constipation. *Cell Host Microbe.* **31**, 1989–2006.e1988 (2023).
62. Li, K. et al. CSN6-SPOP-HMGCS1 axis promotes hepatocellular carcinoma progression via YAP1 activation. *Adv. Sci. (Weinh)* **11**, e2306827 (2024).
63. Fuks, G. et al. Combining 16S rRNA gene variable regions enables high-resolution microbial community profiling. *Microbiome* **6**, 17 (2018).
64. Eisenhofer, R., Minich, J. J., Marotz, C., Cooper, A., Knight, R. & Weyrich, L. S. Contamination in low microbial biomass microbiome studies: issues and recommendations. *Trends Microbiol.* **27**, 105–117 (2019).
65. Li, K. et al. Activation of cyclic adenosine monophosphate pathway increases the sensitivity of cancer cells to the oncolytic virus M1. *Mol. Ther.* **24**, 156–165 (2016).
66. Kumar, S., Stecher, G., Li, M., Knyaz, C. & Tamura, K. MEGA X: Molecular evolutionary genetics analysis across computing platforms. *Mol. Biol. Evol.* **35**, 1547–1549 (2018).
67. Chen, S., Zhou, Y., Chen, Y. & Gu, J. fastp: an ultra-fast all-in-one FASTQ preprocessor. *Bioinformatics* **34**, i884–i890 (2018).
68. Love, M. I., Huber, W. & Anders, S. Moderated estimation of fold change and dispersion for RNA-seq data with DESeq2. *Genome Biol.* **15**, 550 (2014).
69. Subramanian, A. et al. Gene set enrichment analysis: a knowledge-based approach for interpreting genome-wide expression profiles. *Proc. Natl Acad. Sci. USA* **102**, 15545–15550 (2005).

Acknowledgements

We thank Prof. Guangmei Yan (Zhongshan School of Medicine, Sun Yat-sen University), Prof. Yuan Lin (Zhongshan School of Medicine, Sun Yat-sen University), Dr. Minfeng Shu (Shanghai Medical College, Fudan University) and Dr. Jiayu Gu (Shenzhen People's Hospital, The Second Clinical Medical College) for the technical assistance. This research was supported in part by the National Key R&D Program of China (2020YFA0803300, M.H.L.), the National Natural Science Foundation of China (82204411, J.Y.Z., 82473321, K.L. and 82373139, M.H.L.), Postdoctoral Fellowship Program of CPSF (GZB20230887, W.X.W.), the Natural Science Foundation of Guangdong Province (2023A1515030245, K.L. and 2023A1515010737, J.Y.Z.), Guangzhou key research and development program (2023B03J1384, K.L.), the program of Guangdong Provincial Clinical Research Center for Digestive Diseases (2020B1111170004), the Guangzhou Science and Technology Program Project (202206010167), "President Specific Funding" of The Sixth Affiliated Hospital, Sun Yat-sen University, and by the National Key Clinical Discipline, K.L.

Author contributions

J.Y.Z., J.N.Y., J.Y.L., W.L.W., H.D.L., W.X.W., H.M.L.,Y.Z.W., H.R.Y., Y.J.Z., Z.M.F., and H.W.L. carried out the experiments. J.Y.Z. analyzed the data. B.F.Q. performed the ChIP assay. K.L. and M.H.L. obtained funding and provided administrative support for the project. V.P.K., P.Y., T.Z., R.X.Y., H.P.Z., and D.F. provided critical comments. K.L. and M.H.L. conceived the project, directed the research, and co-wrote the paper. All the authors edited and approved the final version of the manuscript.

Competing interests

The authors declare no competing interests.

Additional information

Supplementary information The online version contains supplementary material available at https://doi.org/10.1038/s41467-025-58407-z.

Correspondence and requests for materials should be addressed to Mong-Hong Lee or Kai Li.

Peer review information *Nature Communications* thanks Federica Facciotti, Naziia Kurmasheva and David Olagnier for their contribution to the peer review of this work. A peer review file is available.

Reprints and permissions information is available at http://www.nature.com/reprints

Publisher's note Springer Nature remains neutral with regard to jurisdictional claims in published maps and institutional affiliations.

Open Access This article is licensed under a Creative Commons Attribution-NonCommercial-NoDerivatives 4.0 International License, which permits any non-commercial use, sharing, distribution and reproduction in any medium or format, as long as you give appropriate credit to the original author(s) and the source, provide a link to the Creative Commons licence, and indicate if you modified the licensed material. You do not have permission under this licence to share adapted material derived from this article or parts of it. The images or other third party material in this article are included in the article's Creative Commons licence, unless indicated otherwise in a credit line to the material. If material is not included in the article's Creative Commons licence and your intended use is not permitted by statutory regulation or exceeds the permitted use, you will need to obtain permission directly from the copyright holder. To view a copy of this licence, visit http://creativecommons.org/licenses/by-nc-nd/4.0/.

© The Author(s) 2025